

Neural Representations of Location Composed of Spatially Periodic Bands

Julija Krupic¹, Neil Burgess^{2,3} & John O'Keefe^{1,4*}

1. Dept. of Cell and Developmental Biology, UCL.
2. Inst. of Cognitive Neuroscience, UCL.
3. Inst. of Neurology, UCL.
4. Sainsbury-Wellcome Centre for Neural Circuits and Behaviour, UCL.

*To whom correspondence should be addressed: E-mail: j.okeefe@ucl.ac.uk

The mammalian hippocampal formation provides neuronal representations of environmental location, but the underlying mechanisms are poorly understood. We report a class of cells whose spatially-periodic firing patterns are composed of plane waves (or bands) drawn from a discrete set of orientations and wavelengths. The majority of cells recorded in parasubicular and medial entorhinal cortices of freely-moving rats belonged to this class and included grid cells, an important subset corresponding to 3 bands at 60° orientations and having the most stable firing pattern. Occasional changes between hexagonal and non-hexagonal patterns imply a common underlying mechanism. Our results indicate a Fourier-like spatial analysis underlying neuronal representations of location, and suggest that path integration is performed by integrating displacement along a restricted set of directions.

Grid cells represent the animal's location by firing in a hexagonally symmetric array of locations covering the entire environment(1). They are found in the medial entorhinal cortex (mEC)(1, 2) and in pre- and parasubiculum (PaS)(2). This spatially periodic firing may provide the spatial metric for the hippocampal cognitive map(3–6). The striking hexagonal symmetry raises important questions: is it an entirely unique pattern or one end of a continuum? Is it required for spatial representation or does it reflect properties such as stability(7) or coding efficiency(8)? We recorded 351 cells from superficial layers (II and III) of the medial part of dorsocaudal mEC (5 implants) and adjacent PaS (2 implants) in 7 adult male rats (fig. S1) while they foraged for food in a square enclosure (1.69 m^2). Many of these showed the regular hexagonal pattern characteristic of grid cells (26% passed the standard “gridness” measure(1), Fig. 1A), but a surprisingly large portion (44%) had stable multi-peaked patterns lacking the signature hexagonal symmetry (Fig. 1B,C).

We used two-dimensional Fourier spectral analysis to identify cells whose spatial firing patterns showed significant spatial periodicity(9), being predominantly composed of a small number of Fourier components (i.e. periodic spatial bands with different wavelengths and orientations which sum to produce the firing rate map, Fig. 1F). A cell was categorised as spatially periodic if its strongest Fourier component exceeded 95% of those in spatially shuffled data (fig. S2). Overall 70% of cells were spatially periodic (Fig. 1E, all cells in fig. S3). Of these, 37% were grid cells, usually having three main Fourier components with similar wavelengths, oriented at multiples of 60° from each other (Fig. 1F-G, figs. S4-S8). The remaining spatially periodic cells had one to four main Fourier components with a greater range of relative orientations and wavelengths (Fig. 1G, figs. S6-7, see S8 for comparability of physiological properties). Spatial periodicity might reflect local rather than global spatial structure in the multi-peaked firing fields. Accordingly, we used a second shuffling technique based on shuffling local peak-centred segments of the data. The results show that 144 /154 (94 %) of spatially periodic non-grid cells and 89/91 (98 %) of grid cells had significantly more spatially periodic firing patterns than the $P=0.05$ level in these shuffled data – i.e. significantly more global periodicity than predicted by their local spatial structure ($P<0.01$, binomial probability distribution) (fig. S9) (9). Several cells with one or two main Fourier components (e.g. Fig. 1C, fig. S10) were

reminiscent of the band cells postulated as inputs to grid cells in some computational models (7, 10), see also Refs(11–13).

Could the spatially-periodic non-grid cells provide a consistent metric for an environment comparable to the grid cells? First, we looked at the stability of their firing patterns in familiar environments, between successive trials on the same day and between trials on different days. Spatially-periodic non-grid cell firing patterns were significantly more stable than chance, both within and between days. However, grid cell firing patterns were even more stable than non-grid spatially-periodic cells on both comparisons (see Fig. 2A). The greater stability of grid cell firing patterns corresponded to greater stability in the orientations of their Fourier components (Fig. 2B), suggesting a causal relationship between the two.

Some spatially-periodic cells (11%) changed their firing patterns from grids to non-grids or *vice versa* between trials in the same environment (table S1, fig. S11-12). Figure 2C shows an example of a cell whose firing pattern changed from grid-like to band-like (a simultaneously recorded grid cell remained unchanged, see fig. S12 for details). Such transitions did not reflect unidirectional drift of the grid pattern (sliding time-window spatial autocorrelation analysis, fig. S13). These transitions suggest a continuous population of spatially periodic cells, with grids and non-grids reflecting different combinations of a small set of elemental periodic bands.

A larger proportion of spatially periodic cells (32%) changed between grids and non-grids across different environments (Fig. 2D, table S1) although the majority did not change category (Fig. 2E-F). These transitions corresponded to changing configurations of underlying periodic bands. They did not reflect simpler transformations previously reported for grid cells after environmental manipulations (rotations and translations(14), rescaling(15) or expansions(16)).

Are the spatially periodic cells in one animal composed from the same set of bands? They all tended to have Fourier components clustered around a small number of orientations and wavelengths (figs. S5-7; ref. (15)). As expected, grid cell components were aligned(14, 15) and oriented at 60° to each other (Fig. 3A-G, Rayleigh vector $R_0 = 0.58 \pm 0.14$ for clustering modulo 60°, $P < 0.01$), corroborated by a clustering of the angular separation of neighbouring components around 60° (Fig. 3H, Rayleigh vector $R_0 = 1.1$, $P < 0.001$). The orientations of components of spatially periodic non-grid cells tended to align with those of grid cells (Fig. 3A-

G, fig. S5; mean correlation coefficient 0.54 ± 0.08 , $P < 0.01$ from shuffled data), but included a wider range of relative orientations (Fig. 3I).

If grid cells and spatially periodic non-grid cells are composed of subsets from a larger set of band-like components, there should be examples of simultaneously recorded cells with different components. Fig. 4A,C shows a grid and non-grid spatially periodic cell differing by $\sim 30^\circ$ in the orientation of one of their components (see fig. S14 for more examples). Fig. 4B,D shows two simultaneously recorded grid cells whose three component orientations all differ by $\sim 30^\circ$ and also differ in wavelengths (see fig. S15 for details).

Finally, we asked whether the proportions of grid and spatially periodic non-grid cells differed between the two anatomical regions investigated. Although the overall percentage of spatially periodic cells was lower in mEC (156/239, 65% in mEC; 89/112, 79% in PaS), the proportion of grid cells in mEC (75/156 or 48%) was much higher than in PaS (16/89 or 18%), despite the close anatomical proximity of these regions (fig. S1). This suggests that both regions, with very distinct afferent and efferent connectivity(2, 17, 18), can generate spatially periodic cells, albeit with major differences in the prevalence of pure hexagonal symmetry. In both regions, cell firing shows strong theta modulation: 67% of all spatially periodic cells were theta-modulated in PaS (mean frequency 9.2 ± 0.1 Hz; 65% of all cells were theta-modulated), and 56% in mEC (with similar mean frequency; 47% of all cells were theta-modulated), pointing to a common characteristic of spatially periodic cells regardless of their anatomical location (fig. S16).

The abrupt increase in the proportion of grid cells in mEC suggests that mEC has micro-circuitry or anatomical inputs organized to prefer components at 60° angles, which in turn provides the most stable inputs to the hippocampus. In contrast, PaS, with a higher proportion of spatially periodic cells, but more varied and less stable firing patterns, receives one of its major afferents from the hippocampus and heavily projects to the superficial layers of mEC(17, 19) and may represent an intermediate stage in constructing stable grids from periodic bands.

The heterogeneous spatially periodic firing patterns reported here could reflect a common process of self-organisation acting on ‘band cells’ upstream of the recorded cells(7, 10). The most stable outcome of such a process would be hexagonal grids(10), while mixtures of orientations organised at multiples of around 30° and 60° can also be stable(7) and might support multi-scale representation(4, 20). What mechanism might underlie the bands? Theta-modulated

firing reminds us that theta rhythmicity controls the scale of spatial representations(21–23) and that interference between theta oscillations could integrate self-motion to produce band-like firing patterns which drive grid cell firing(10–12). These band cells might correspond to phase modulated firing from “theta cells” in the septo-hippocampal circuit(13) or be generated by one dimensional ring attractors(7, 24). Alternatively, in the attractor model(4, 6, 25) recurrent interactions between grid cells could produce a stable grid-like as well as periodic band-like “Turing” pattern(6, 26) of firing across a sheet of cells, which translates into their spatial firing as the animal moves.

In summary, the firing patterns of the majority of cells recorded in parasubicular and medial entorhinal cortices showed a stable spatial periodicity described by superposition of a small number (up to four) of elemental periodic band-like components drawn from a discrete set of orientations and wavelengths. Grid cells correspond to hexagonal configurations, which have the greatest spatial stability. Our results suggest that path integration is performed by integrating self-motion along a restricted set of directions, mediated by planar periodic representations (bands) of multiple scales along each direction, and that self-organisation of these band-like inputs may underlie the firing of all spatially periodic cells in the parahippocampal region.

Fig. 1. Spatial periodicity of neuronal firing patterns. **(A-D)** Firing rate maps (top row), trajectory (black) with spike positions (red) (second row), spatial autocorrelograms (third row) and 2D Fourier spectrograms (bottom row) for two successive trials of the same cell in a $1.3 \times 1.3 \text{m}^2$ enclosure. **(A-C)** Spatially-periodic cells. The cell in **(A)** qualifies as a grid cell, the cell in **(B)** fires in an irregular grid, **(C)** has a more band-like firing pattern. **(D)** A non spatially-periodic cell. Peak firing rate, gridness and maximum Fourier power shown (top left of the corresponding plots). Rate map stability between trials is indicated above. **(E)** Distribution of cell types in dorsal mEC and adjacent PaS. Left: all cells, divided into spatially-periodic (SPC) and non spatially-periodic (nonSPC) cells. Right: spatially-periodic cells only, divided into grid cells (GC), conjunctive grid cells (conj. GC), SPCs with a head-direction correlate (HD) and other SPCs. **(F)** Two dimensional Fourier analysis. Left: the centred two dimensional Fourier spectrogram of the rate map shown in **(A, left)**, with main Fourier components shown at the sides with corresponding wave vectors (white arrows). Right: the spectrogram shows the power corresponding to plane waves (wave vector \mathbf{k}) at (l_x, l_y) from the centre. The periodic bands in the plane wave are oriented perpendicular to the wave vector \mathbf{k} and their wavelength is inversely proportional to its length. **(G)** Distribution of the number of main Fourier components across spatially-periodic cells (non-grid cells in red, grid cells in black).

Fig. 2. Stability of spatially-periodic cell firing. **(A)** Grid cells, GC, were more stable than spatially-periodic non-grid cells, nonGC, and both were superior to nonspatially-periodic cells, nonSPC, both between sessions on the same day in the same environment (left, GC: $r = 0.54 \pm 0.02$ (mean \pm s.e.m.), nonGC: $r = 0.45 \pm 0.02$, nonSPC: $r = 0.21 \pm 0.03$, $P_{144}(\text{GC}>\text{nonGC}) = 0.015$, $P_{78}(\text{GC}>\text{nonSPC}) = 0.65\text{e-}012$, $P_{125}(\text{nonGC}>\text{nonSPC}) = 1.69\text{e-}010$, paired t-tests, one-tailed) and across days (right, GC: $r = 0.53 \pm 0.03$, nonGC: $r = 0.44 \pm 0.04$, nonSPC: $r = 0.18 \pm 0.03$, $P_{51}(\text{GC}>\text{nonGC}) = 0.049$, $P_{24}(\text{GC}>\text{nonSPC}) = 1.39\text{e-}005$, $P_{41}(\text{nonGC}>\text{nonSPC}) = 3.14\text{e-}004$; paired t-tests, one-tailed). **(B)** Fourier polar component stability mirrored rate map stability inter-session (left, GC > nonGC: $r = 0.73 \pm 0.04 > r = 0.51 \pm 0.03$, $P_{144} = 3.24\text{e-}005$, paired t-tests, one-tailed) and inter-day (right: 0.70 ± 0.06 vs. 0.47 ± 0.07 , $P_{24} = 0.015$, paired t-tests, one-tailed). Occasionally, cell firing altered between grid and non-grid patterns between trials, **(C)**, in the same environment or **(D)**,

in different environments. More often, the structure of grids, (E), and spatially-periodic non-grids, (F), was maintained across environments.

Fig. 3. Orientations of main Fourier components within each animal. (A-G) Histograms of the orientations of main Fourier components of the spatially-periodic cells recorded in each animal (in a $1.3 \times 1.3 \text{ m}^2$ enclosure; non-grid cells in red; grid cells in black). (A-B) cells in PaS; (C-G) cells in mEC (A: r1682; B: r1738; C: r1728; D: r1709; E: r1737; F: r1739; G: r1710). Distribution of the relative orientations of Fourier components of all grid cells, (H), and all spatially-periodic non-grid cells, (I).

Fig. 4. Spatially-periodic cells with different Fourier components co-exist within the same animal. (A) Simultaneously recorded grid cell (top) and spatially-periodic non-grid cell (bottom) with one Fourier component misaligned between the two (r1738). (B) Simultaneously recorded grid cells of different scale and orientation (r1737). Left to right: firing rate map, spatial autocorrelogram, 2D Fourier spectrogram with peak firing rate, gridness score and maximum Fourier power indicated on the top left of the corresponding plots. (C) The orientations of the main Fourier components in (A) superimposed (colors as in A). (D) The mean orientations of the main Fourier components (fig. S15) in (B) (colors as in B). (E) Wavelength distribution of Fourier components of simultaneously recorded grid cells with the same orientations as the cell in (B, top; red) and the cell in (B, bottom; blue). The mean wavelength for each module is indicated above. Their ratio is ~ 1.57 .

References and Notes

1. T. Hafting, M. Fyhn, S. Molden, M.-B. Moser, E. I. Moser, *Nature* **436**, 801–806 (2005).
2. C. N. Boccara *et al.*, *Nat Neurosci* **13**, 987–994 (2010).
3. J. O’Keefe, L. Nadel, *The Hippocampus as a Cognitive Map* (Oxford University Press, 1978).
4. I. R. Fiete, Y. Burak, T. Brookings, *J. Neurosci.* **28**, 6858–6871 (2008).
5. J. O’Keefe, N. Burgess, *Hippocampus* **15**, 853–866 (2005).
6. B. L. McNaughton, F. P. Battaglia, O. Jensen, E. I. Moser, M.-B. Moser, *Nat Rev Neurosci* **7**, 663–678 (2006).
7. H. Mhatre, A. Gorchetchnikov, S. Grossberg, *Hippocampus* **22**, 320–334 (2012).
8. S. Sreenivasan, I. Fiete, *Nat Neurosci* **14**, 1330–1337 (2011).
9. Materials and methods are available as supporting material on Science Online.
10. N. Burgess, C. Barry, J. O’Keefe, *Hippocampus* **17**, 801–812 (2007).
11. N. Burgess, *Hippocampus* **18**, 1157–1174 (2008).
12. M. E. Hasselmo, *Hippocampus* **18**, 1213–1229 (2008).
13. A. C. Welday, I. G. Shlifer, M. L. Bloom, K. Zhang, H. T. Blair, *J. Neurosci.* **31**, 16157–16176 (2011).
14. M. Fyhn, T. Hafting, A. Treves, M.-B. Moser, E. I. Moser, *Nature* **446**, 190–194 (2007).
15. C. Barry, R. Hayman, N. Burgess, K. J. Jeffery, *Nat Neurosci.* **10**, 682–684 (2007).
16. C. Barry, J. O’Keefe, N. Burgess, *SfN abstract* **35**, 101.24 (2009).
17. C. F. Doeller, C. Barry, N. Burgess, *Nature* **463**, 657–661 (2010).
18. T. van Groen, J. M. Wyss, *Brain Research* **518**, 227–243 (1990).
19. A. Burgalossi *et al.*, *Neuron* **70**, 773–786 (2011).
20. C. Köhler, *J. Comp. Neurol.* **236**, 504–522 (1985).
21. H. T. Blair, A. C. Welday, K. Zhang, *J. Neurosci.* **27**, 3211–3229 (2007).

22. A. P. Maurer, S. R. VanRhoads, G. R. Sutherland, P. Lipa, B. L. McNaughton, *Hippocampus* **15**, 841–852 (2005).

23. C. Geisler, D. Robbe, M. Zugaro, A. Sirota, G. Buzsáki, *PNAS* **104**, 8149–8154 (2007).

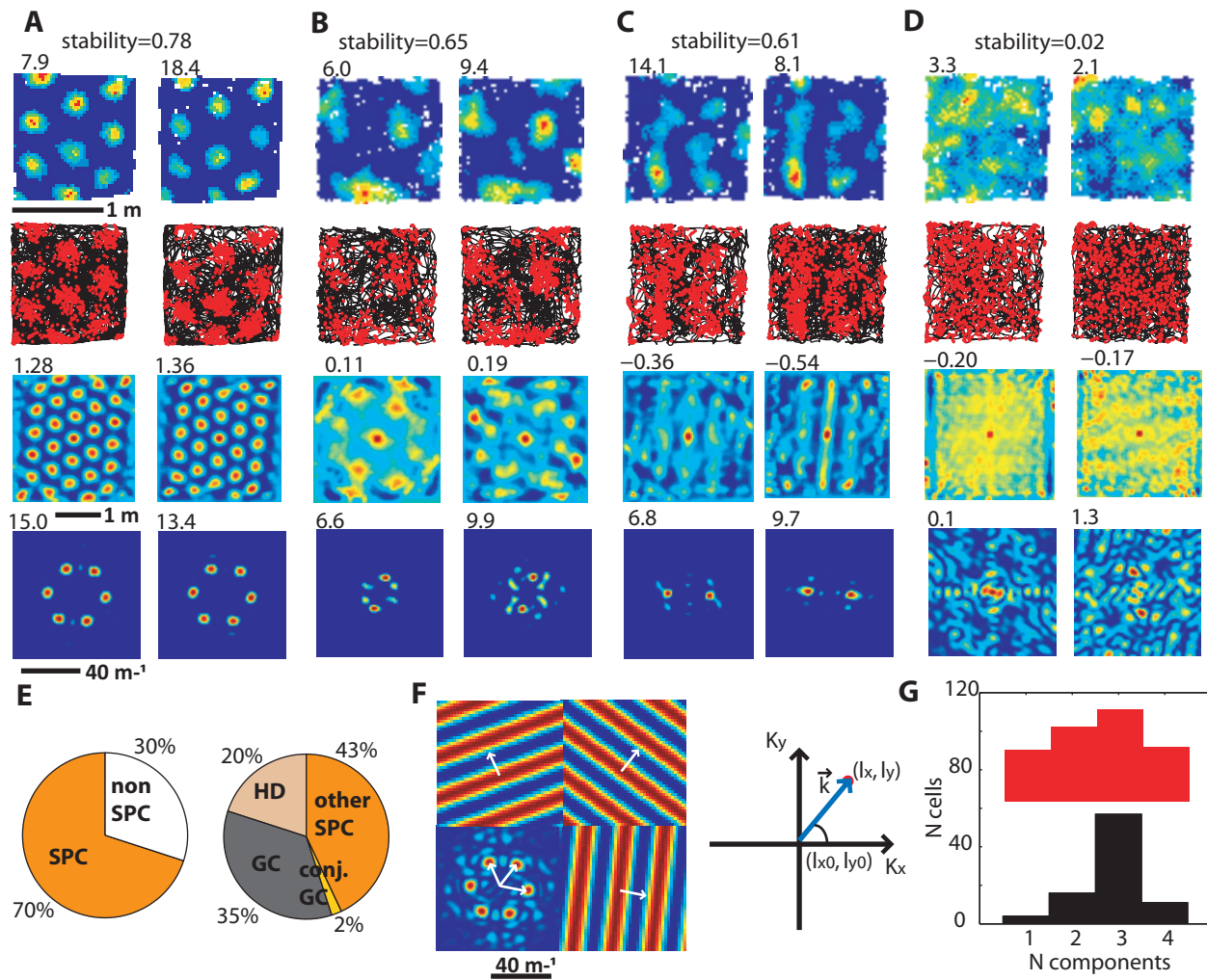
24. J. O’Keefe, M. L. Recce, *Hippocampus* **3**, 317–330 (1993).

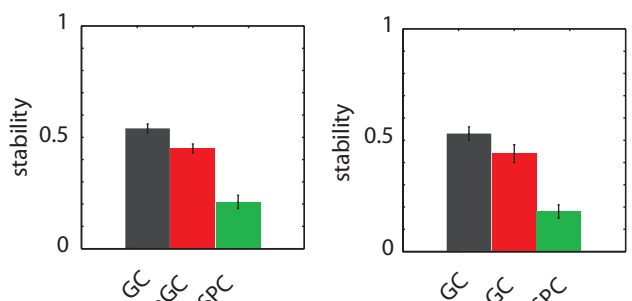
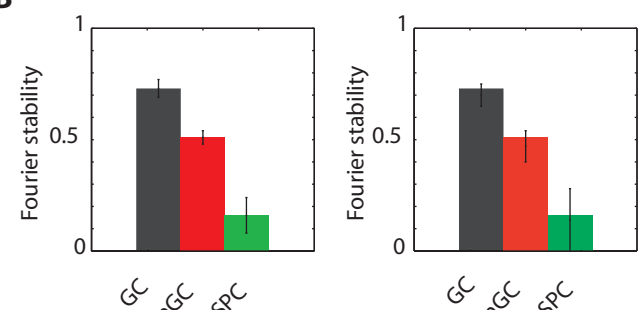
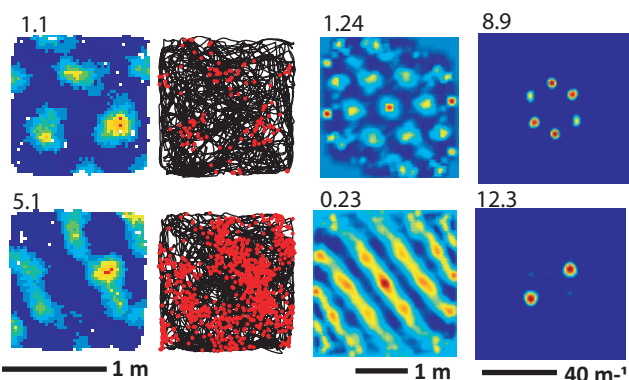
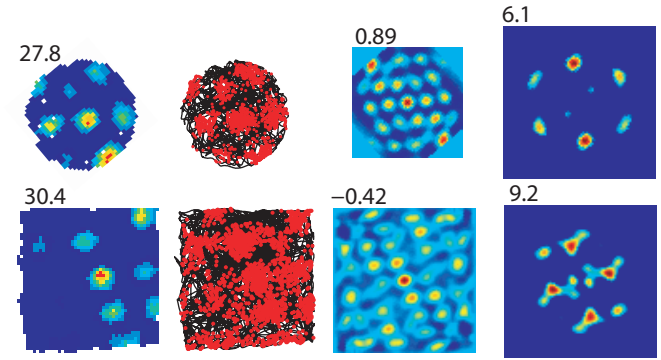
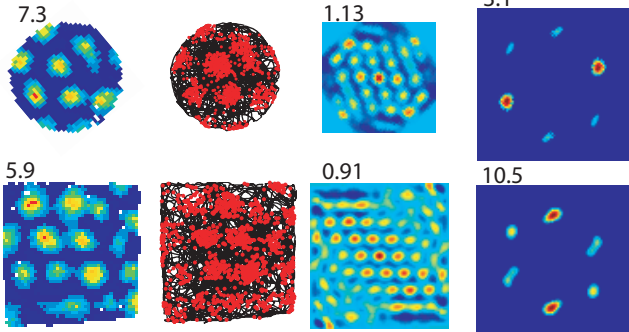
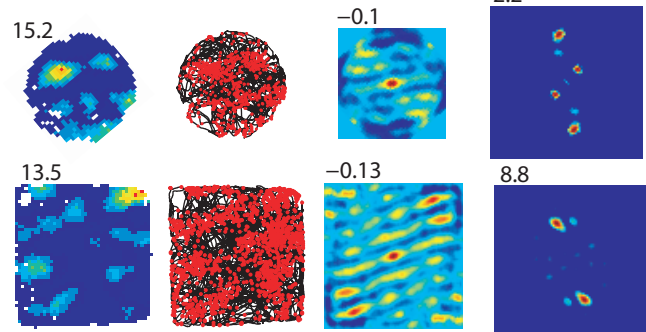
25. H. T. Blair, K. Gupta, K. Zhang, *Hippocampus* **18**, 1239–1255 (2008).

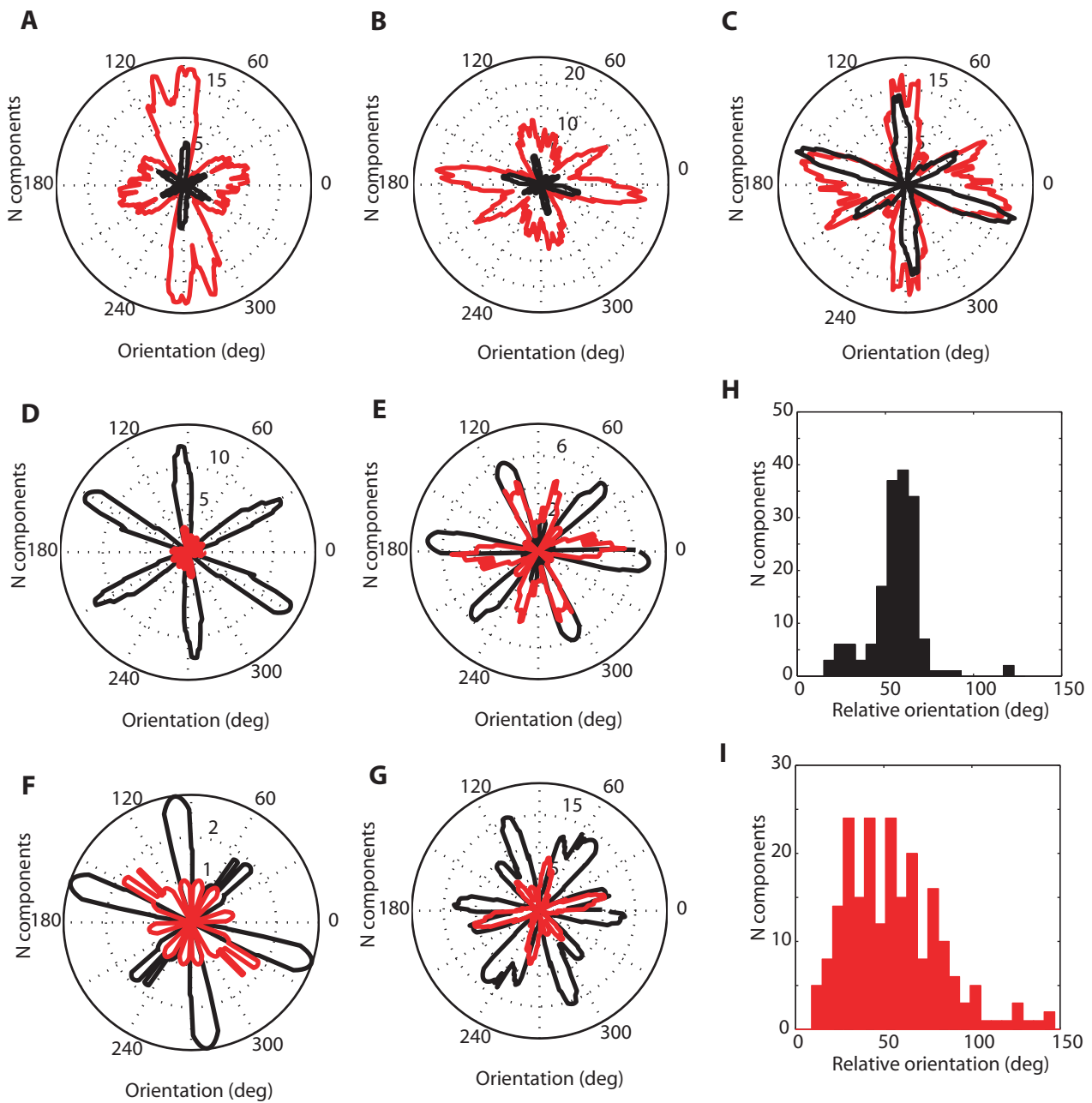
26. M. C. Fuhs, D. S. Touretzky, *J. Neurosci.* **26**, 4266–4276 (2006).

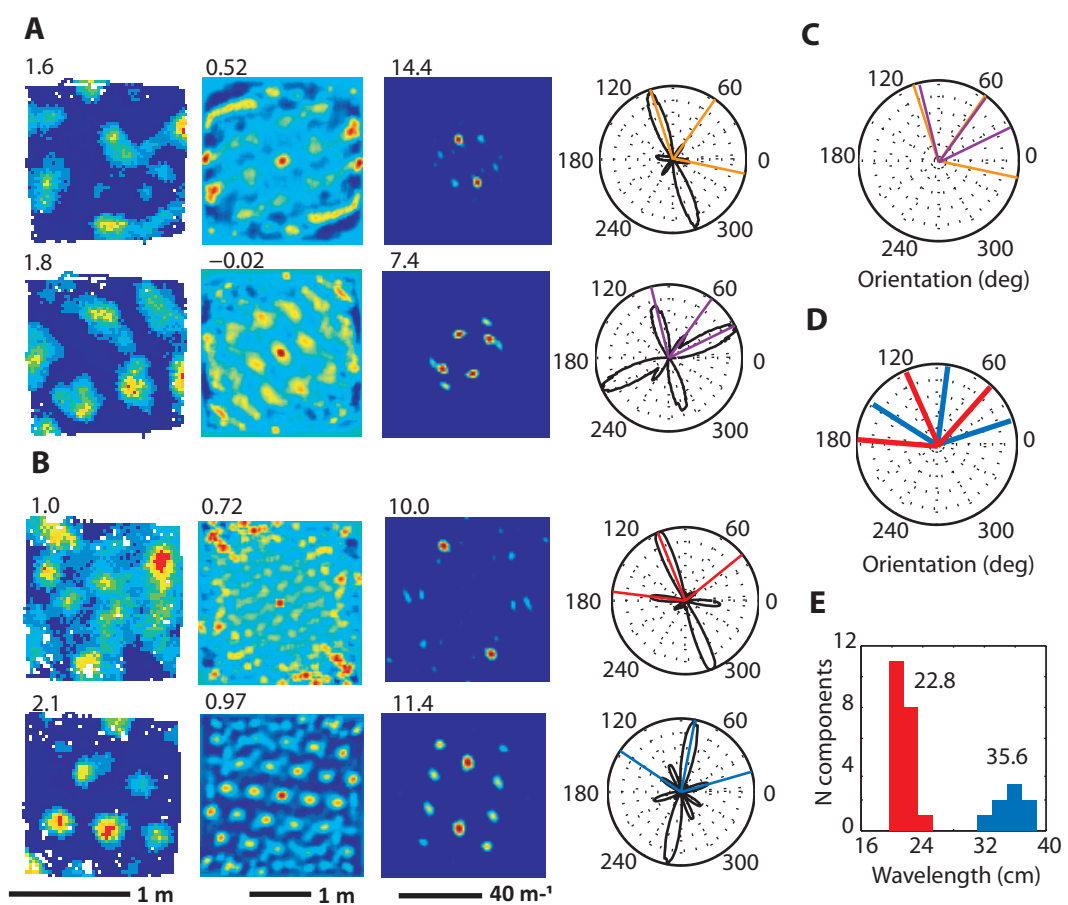
27. P. Borckmans *et al.*, *Int. J. of Bifurcat. Chaos* **12**, 2307–2332 (2002).

28. Supported by the E.U. Framework 7 (SPACEBRAIN) grant, U.K. Medical Research Council, Gatsby Charitable Foundation, and Wellcome Trust. JK received support from a CoMPLEX studentship. The authors would like to thank M. Bauza, T. Wills, C. Barry, F. Cacucci and M. Witter for useful discussions; S. Burton for help with histology. Work was conducted in accordance with the UK Animals (Scientific Procedures) Act, 1986.



A**B****C****D****E****F**





	Same environment	Different environment
No change occurred	40 cells (89%, N=45)	19 cells (68%, N=28)
Change occurred	5 cells (11%, N=45)	9 cells (32%, N=28)

Table S1. The frequency of changes in spatially periodic firing between grid and non-grid patterns in the same (1 m circle or 1.3 m square) enclosure and across different environments (from 1 m circle to 1.3 m square enclosure). The 9/28 cells showing a change between environments is significantly above that expected from the spontaneous rate of change in the same environment (11%), $p=0.002$ (binomial test).

Supporting Materials

This PDF includes:

Materials and Methods

figs. S1 to S16

References (1-7)

Materials and Methods

Subjects

Seven male Lister Hooded adult rats were used for the experiments. Rats were individually housed in clear plastic cages (68 cm x 44 cm x 48 cm, W x L x H) and were kept on a 12:12 hours light:dark cycle at a controlled temperature (19-23 °C) and humidity (50-70 %). The rats weighed 350-380g on the day of surgery. They were maintained on a 90% of body weight food deprivation schedule where the most recent feeding was at least 12 hours before the experiments. Water was supplied ad libitum.

Surgery and electrodes

The rats were anaesthetised with 1-3 % of isoflurane in O₂ and an 0.01mg /100g im injection of buprenorphine. They were chronically implanted in the left hemisphere with a microdrive loaded with four tetrodes (HM-L coated 90 % platinum and-10 % iridium 17 microns diameter wire). The tetrodes were tightly glued together and cut at the same level. The electrode tips were plated to reduce the impedance to 150-300 kΩ at 1 kHz. Tetrodes were aimed at the superficial layers of medial part of dorsocaudal medial entorhinal cortex (mEC) and adjacent parasubiculum (PaS) (4.3 mm lateral to the midline; 0.3 mm anterior to the sinus and 1.5 mm below the pia). Six screws were threaded into the skull and the microdrive anchored to them with dental cement. A jeweller's screw fixed to the skull over the opposite hemisphere was

used as a ground screw. After surgery the rats were given at least 7 days to recover before the experiments were started.

Histology and electrode localization

After completion of the recording sessions the rats were sacrificed using an overdose of sodium pentobarbital and perfused transcardially with saline followed by 4 % of paraformaldehyde (PFA). The brain was cryoprotected in 4 % PFA and 20 % sucrose solution and sliced into 30 micron parasagittal sections using a freezing microtome. Sections were mounted and Cresyl-Violet Nissl-stained to allow visualization of the electrode track. Recording sites were determined by measuring backwards from the deepest point of the track and ensuring that the total length of the electrode track corresponded to the amount of electrode movement as measured from the microdrive screw turns (fig. S1). 20 % shrinkage was allowed. mEC layer II cells were identified as a densely packed strongly stained layer of cells. mEC layer III cells were less intensely stained and less densely packed. PaS superficial layers cells were identified as densely packed cells located in a dorsocaudal area above superficial layers of mEC which showed less staining and did not show a clear laminar structure.

Data Collection

Rats were allowed at least 7 days of recovery after surgery. Tetrodes were lowered 50 microns or less per day at the end of each recording session until the first cells of interest were found. Single unit data were acquired using a proprietary data acquisition system. Two infrared LEDs of different intensities and separated by 7 cm were fixed on the animal's head in order to track the animal's position and head orientation. The (x, y) coordinates of the LEDs were acquired at 50 Hz by an infrared camera attached to the ceiling above the centre of the environment.

Single cell isolation from multi-unit recordings

Isolation of single units was performed by manual cluster-cutting. Clusters were isolated in a feature space where all possible combinations of pairs of spike amplitudes recorded by four tetrodes were plotted against each other. Unit isolation was further refined by taking into account additional properties of spike waveforms such as the existence of positive pre-potentials. The quality of cluster isolation was tested by estimating the L-ratio and isolation distance(*I*) (fig. S8). The isolation distance shows how distant the cluster spikes are compared to other spikes recorded by the tetrode in Mahalanobis space. L-ratio indicates the number of ‘noise spikes’ (i.e. spikes which are not part of the cluster) in the vicinity of the cluster. L-ratio reflects the number of spikes that could belong to a cluster but were not included, whereas isolation distance reflects the amount of potential ‘noise spikes’ included into the cluster. Clusters recorded on different trials were assigned to the same cell if: a) the tetrode had not been moved between trials; b) there was minimal change in spike waveforms; c) the position of the target cluster and neighbouring clusters remained similar in feature space.

Training procedures and testing environments

The animals were recorded in a familiar square (1.3 m x 1.3 m x 0.5 m) enclosure. The sides of the wooden square enclosure were painted in light grey and the bottom in dark grey. The recording enclosure was always placed in the same position with respect to the laboratory. Distal visual cues (e.g. a white rectangular cue card, shelves, recording system etc) were available to maintain the same allocentric orientation across the trials. The animals were trained to forage for sweetened rice thrown into random locations in the enclosure approximately every 10-20 seconds. At least two 15 min trials were recorded within a day. There were 10 min intervals between every trial during which the animal rested on a holding platform located near the testing environment.

To ensure that our observations did not result from an inadequate spatial sampling resolution, for two rats (r1738 and r1739) we used a higher resolution camera (360 pixels/m) and ran longer trials (at least 30 min) in addition to the usual camera (214

pixels/m) and duration used for all the other rats. The enhanced resolution and duration recordings did not show any differences in cell firing patterns.

In some of the sessions we also run a 10-15 min trial in which the animal foraged in a familiar 1 m diameter x 0.5 m circular enclosure.

We ran trials in the dark as well as the light but only the light trials were included in our final analysis. All the first trials of the day were excluded to minimise novelty effects.

Criteria for cell inclusion

Cells were included in the final analysis if they satisfied the following criteria: a) the animal was familiar with the testing environment: defined as having previous exposure of at least five 20 min trials recorded within at least 3 days; b) the cell was recorded for at least two trials; c) it had a spike width $> 200 \mu\text{s}$ (fig. S8); d) fired at least 100 spikes within the trial and e) had a peak firing rate $> 1 \text{ Hz}$ and a mean firing rate $< 5 \text{ Hz}$ (fig. S8).

Firing rate maps

Locational firing rate map was estimated by dividing the number of spikes fired in a given part of the environment by the time spent there. Position data and spike counts were sorted into 2.5cm x 2.5cm spatial bins. Unsmoothed firing rate maps were obtained by dividing the spike count in each bin by the dwell time in that bin. The smoothed firing rate map was obtained by first applying adaptive smoothing (see ‘Adaptive Smoothing’) to the dwell time and spike maps and then dividing them. Color bars represent firing rate in deciles of the range of firing rates (top 10 % in red, bottom 10 % in blue). Unvisited bins are shown in white.

Directional firing rate was estimated by dividing spike counts and dwell time into 3 degree bins). Adaptive smoothing was applied to spike and dwell time maps before dividing them.

Adaptive smoothing

Adaptive smoothing(2) was applied to the firing rate maps. In brief, to calculate the firing rate for a given bin the number of spikes assigned to that bin is defined by a circle centred at the bin with the radius r . The radius of the circle is expanded until

$$r \geq \frac{\alpha}{n\sqrt{s}} \quad (1)$$

where $\alpha = 5000$, n is the number of bins and s is the number of spikes lying within the circle.

Assessing cells with spatially periodic firing patterns

To estimate the degree of periodic regularity in the spatial distribution of cell firing we calculated the two-dimensional Fourier spectrogram:

$$F[l_y, l_x] = \frac{1}{fr_{mean} \sqrt{M_x N_y}} \sum_{n=0}^{N-1} \sum_{m=0}^{M-1} f[m, n] e^{-2\pi i \left(\frac{ml_y}{M} + \frac{nl_x}{N} \right)} \quad (2)$$

where $i = \sqrt{-1}$, and $f[m, n]$ is the unsmoothed firing rate map, with mean firing rate subtracted, zero-padded to have size $M_x \times N_y = 256 \times 256$ to increase the spatial resolution of the Fourier spectrogram. The spectrogram is a matrix of Fourier coefficients corresponding to a basis set of plane waves of varying wavelength and orientation (Fig. 1F). Each plane wave is specified by the integer values (l_y, l_x) which identify the y and x components of the wave vector in terms of the number of spatial cycles covering the entire firing rate map along its height and its width respectively (see equation 6, below). fr_{mean} is the mean firing rate (the total number of spikes divided by trial duration). M_x and N_y are the width and length in bins of the original firing rate map before zero-padding. Division by $\sqrt{M_x N_y}$ enables comparison of Fourier power between firing rate

maps from different size environments. Normalising by mean firing rate enables comparison of cells with different firing rates.

The power of the Fourier spectrum is calculated as

$$P[l_y, l_x] = \sqrt{F_r^2[l_y, l_x] + F_i^2[l_y, l_x]} \quad (3)$$

where F_r and F_i are the real and the imaginary parts of Fourier spectrum respectively.

The maximum Fourier power $P[l_x, l_y]$ of the firing pattern was used to assess the degree of its spatial periodicity.

Estimating and displaying spatial periodicity

We used the shift property of two-dimensional Fourier spectrograms to shift low frequencies to the centre and high frequencies to the periphery of the Fourier spectrogram by changing the signs of all points in the rate map $f[m, n]$:

$$f'[m, n] = f[m, n](-1)^{m+n} \quad (4)$$

and applied equations (2) and (3) to $f'[m, n]$ to obtain the centred Fourier spectrogram.

The wave vector corresponding to point (l_y, l_x) in the spectrogram is:

$$k_y = \frac{2\pi(l_y - l_{cy})}{Mb}; \quad k_x = \frac{2\pi(l_x - l_{cx})}{Nb} \quad (5)$$

where (l_{cy}, l_{cx}) is the coordinate of the centre of the spectrogram, and b is the bin size in meters. The corresponding spatial wavelengths are:

$$\lambda_y = \frac{2\pi}{k_y}; \quad \lambda_x = \frac{2\pi}{k_x}. \quad (6)$$

The overall wavelength is:

$$\lambda = \sqrt{\lambda_x^2 + \lambda_y^2} \quad (7)$$

and the direction of the wave vector is

$$\varphi = \text{atan} \left(\frac{k_y}{k_x} \right). \quad (8)$$

Hence the direction of the orientation of the periodic bands is:

$$\theta = \varphi + 90^\circ \quad (9)$$

Defining the main Fourier components of spatially periodic cells

We estimated the presence of the main plane-wave Fourier components in the two dimensional Fourier spectrograms as follows. To reduce effects of noise the 50th percentile value of power in shuffled data was subtracted from the two dimensional Fourier spectrogram and negative values set to zero. To exclude spatial sub-harmonic main components had to be larger than 10% of the maximum power in the polar Fourier spectrogram (obtained from the two dimensional Fourier spectrogram after removal of the 50th percentile shuffled power value). Main peaks with orientations within 10 degrees of a higher peak were ignored to rule out local maxima. Around 6% of the spatially periodic cells had more than 4 components (not shown in Figs. 1,3) and were not included into the final analysis, since most of the time they resulted from an error in estimating the number of components (e.g. the sub-harmonic frequencies were included etc). All of the spatially periodic cells with all of their components are shown in fig. S3.

Assessing “gridness”

Gridness was obtained as in (5). We calculated the spatial autocorrelogram as

$$r(\tau_x, \tau_y) = \frac{n \sum f(x, y) f(x - \tau_x, y - \tau_y) - \sum f(x, y) \sum f(x - \tau_x, y - \tau_y)}{\sqrt{n \sum f(x, y)^2 - (\sum f(x, y))^2} \sqrt{n \sum f(x - \tau_x, y - \tau_y)^2 - (\sum f(x - \tau_x, y - \tau_y))^2}} \quad (10)$$

where $r(\tau_x, \tau_y)$ the autocorrelation between bins with spatial offset τ_x and τ_y . f is the firing rate map of the cell with no smoothing applied; n is the number of overlapping bins

in two offset copies of the map. The autocorrelogram was smoothed using a two-dimensional Gaussian kernel of 5 bins with standard deviation equal to 2 bins. The six local peaks of the autocorrelogram were defined as the six local maxima with $r > 0$ closest to the central peak (excluding the central peak itself). Gridness was calculated by defining a mask on the spatial autocorrelogram centred on the central peak but excluding the peak itself bounded by a circle defined by the mean distance from the centre to the closest peaks multiplied by 2.5. This area was rotated in 30 degrees increments up to 150 degrees and for each rotation the Pearson product-moment correlation coefficient was calculated against the un-rotated mask. Gridness is then calculated taking the difference between the minimum correlation coefficient for rotations of 60 and 120 degrees and the maximum correlation coefficient for rotations of 30, 90 and 150 degrees.

Assessing directional modulation of cell firing

The uni-modal directionality of cell firing was evaluated using the Rayleigh vector, i.e. the length of the mean resultant vector calculated from the binned and smoothed polar rate map.

Criteria for cell classification

All cell types were identified by comparing a relevant measure to a threshold value calculated as the 95th percentile value of shuffled data (fig. S2). The data was shuffled(3) by wrapping the time-shifted spike train around the position data. The spike train was shifted by a random duration more than 20 s and less than trial duration minus 20s. Cells were classified as spatially periodic based on the maximum power of their two dimensional Fourier spectrogram; cells were classified as grid cells based on their gridness score; cells were classified as directional cells based on the length of their Rayleigh vector. The shuffling was performed on all cells, on a cell-by-cell basis, until the 95th percentile of the maximum power Fourier component converged to a constant.

Estimating the significance of spatial regularity, given preserved local structure

As well as using spike-shuffling to assess the significance of spatial periodicity in cell firing, see above, we also estimated the significance of spatial periodicity in firing maps

under a Null Hypothesis that local spatial structure (i.e. local peaks in firing) is preserved and randomly distributed across the environment. To do this, we found the local maxima of the smoothed rate map (see ‘Adaptive Smoothing’), and used these as the centers of Voronoi polygons (4) tessellating the environment (see fig. S9A,D). To create spatially shuffled data, the Voronoi polygons were rotated by random amounts from 0 to 360 degrees, and their centers assigned to coordinates randomly selected from zero to the side length of the environment. A shuffled unsmoothed rate map was constructed as a surrogate for the cell’s unsmoothed rate map by moving the data in each bin according to the movement of its corresponding polygon, as described above. Where polygons overlapped, the newest value was assigned to the bin. Bins falling outside of the arena were randomly assigned to unused bins within the arena. (NB the two dimensional Fourier spectrograms of firing maps are divided by the sum over all the bins from the unsmoothed firing rate to compensate for any differences in Fourier power due to differences in firing rate, such as that due to the loss of overlapping bins.) The peak Fourier power in the spectrogram was calculated, as above. The shuffling was performed on all cells, on a cell-by-cell basis, until the 95th percentile of the maximum power Fourier component converged to a constant.

The wavelength distribution of all main Fourier components

The wavelength of a main Fourier component was calculated by first obtaining its orientation from the polar Fourier spectrogram and then making a ‘line mask’ aligned along this orientation in the two dimensional Fourier spectrogram (i.e. only the Fourier power laying along the orientation and starting on the centre of the spectrogram were taken into account). The maximum point on the mask was taken as the wavelength.

Wavelength clustering of all main Fourier components

To evaluate how clustered the wavelengths were we applied K-means clustering of the wavelengths of all the main Fourier components for each animal (nonGCs and GCs were combined). The number of clusters (K) was chosen from 2 to 4 (judging by eye from fig. S5). The tightness of the K clusters was evaluated by calculating the standard deviation of the points in the cluster and comparing it to the 95th percentile of the smallest standard deviation of randomly shuffled points. The number of points shuffled was equal

to the number of data points and the number of clusters (K) applied to the surrogate data was the same as the number applied to the real data. Clusters with wavelengths comparable to the side length of the square environment were not evaluated since these wavelengths would show artificially high variability due to sampling limitations (according to the Nyquist sampling theorem, wavelengths larger than half of the environment cannot be sampled precisely).

The polar distribution of Fourier power

To study the distribution of Fourier power over orientations it was convenient to display the two dimensional Fourier spectrogram as a polar plot, referred to as a Fourier polar plot (fig. S4). In this plot the mean power from all wavelengths at a given orientation was calculated for all orientations, smoothed using a Gaussian kernel with width 17 degrees (standard deviation = 13 degrees).

Distribution of orientations of the main Fourier components

The distribution of the orientations of all the main Fourier components of spatially periodic cells was also smoothed using Gaussian kernel with width 17 degrees (standard deviation = 13 degree).

Assessing 60° clustering of the absolute and relative orientations of Fourier components

To test for clustering of the orientations of the main Fourier components of the grid cells within an animal at multiples of 60°, we found the distribution of orientations modulo 60° and mapped this onto 360° (i.e. orientation θ became $360(\theta \bmod 60)/60$). We then calculated the Rayleigh vector R to assess the extent of uni-modal clustering at this modulo angle.

A similar procedure was used to test for 60° clustering of the relative orientations of neighbouring Fourier components (Fig. 3H).

Stability of the rate map and Fourier-components of spatially periodic cells

To estimate the inter-session and inter-day stability respectively we calculated the Pearson product-moment correlation coefficient between the rate maps of two consequent trials within the same day and between the rate maps of the first available trials across two consequent recording.

In addition, to evaluate the stability of the orientations of main Fourier components we calculated the Pearson product-moment correlation coefficient between the Fourier polar plots. Unlike the stability measure obtained from rate maps, this stability measure is not sensitive to the changes in firing rates of individual fields or to translations of the firing pattern.

Calculating time-windowed spatial autocorrelograms

The standard spatial autocorrelogram represents the probability of pairs of spikes occurring with a specific displacement (x,y) displayed as a function of (x,y), calculated over locational bins to allow normalisation by dwell time. Time-windowed spatial autocorrelograms represent the same information, but restricted to pairs of spikes fired within a specific time of each other. We calculated the gridness score of spatially periodic cells from the time-windowed spatial autocorrelogram in the normal way (using the 'ring mask' obtained from the whole trial spatial autocorrelogram, see above), and examined how it changes as we increase the duration of the sliding time-window (fig. S13).

Estimating theta modulation of cell firing

The degree of theta modulation was estimated by obtaining the unsmoothed temporal autocorrelogram of the cell's spike train for time delays ranging from 1 to 500 ms with a bin size of 1ms. The autocorrelogram was zero-padded from 500 bins to 2^{13} bins to enhance the temporal resolution of the one-dimensional Fourier spectrogram. Similar to criteria described previously(3, 6, 7), a cell was considered theta modulated if the mean power within 1 Hz of the peak in the 6-10 Hz range was at least 4 times greater than the mean power in the 2-125 Hz range.

References

1. N. Schmitzer-Torbert, J. Jackson, D. Henze, K. Harris, A. D. Redish, Quantitative measures of cluster quality for use in extracellular recordings, *Neuroscience* **131**, 1–11 (2005).
2. W. E. Skaggs, B. L. McNaughton, K. M. Gothard, E. J. Markus, An Information-Theoretic Approach to Deciphering the Hippocampal Code, *IN* **5**, 1030–1037 (1993).
3. T. J. Wills, F. Cacucci, N. Burgess, J. O'Keefe, Development of the Hippocampal Cognitive Map in Preweanling Rats, *Science* **328**, 1573–1576 (2010).
4. G. Voronoi, Nouvelles applications des paramètres continus à la théorie des formes quadratiques, *Journal für die Reine und Angewandte Mathematik* **133**, 97–178 (1908).
5. T. Hafting, M. Fyhn, S. Molden, M.-B. Moser, E. I. Moser, Microstructure of a spatial map in the entorhinal cortex, *Nature* **436**, 801–806 (2005).
6. C. N. Boccara *et al.*, Grid cells in pre- and parasubiculum, *Nat Neurosci* **13**, 987–994 (2010).
7. R. F. Langston *et al.*, Development of the Spatial Representation System in the Rat, *Science* **328**, 1576–1580 (2010).

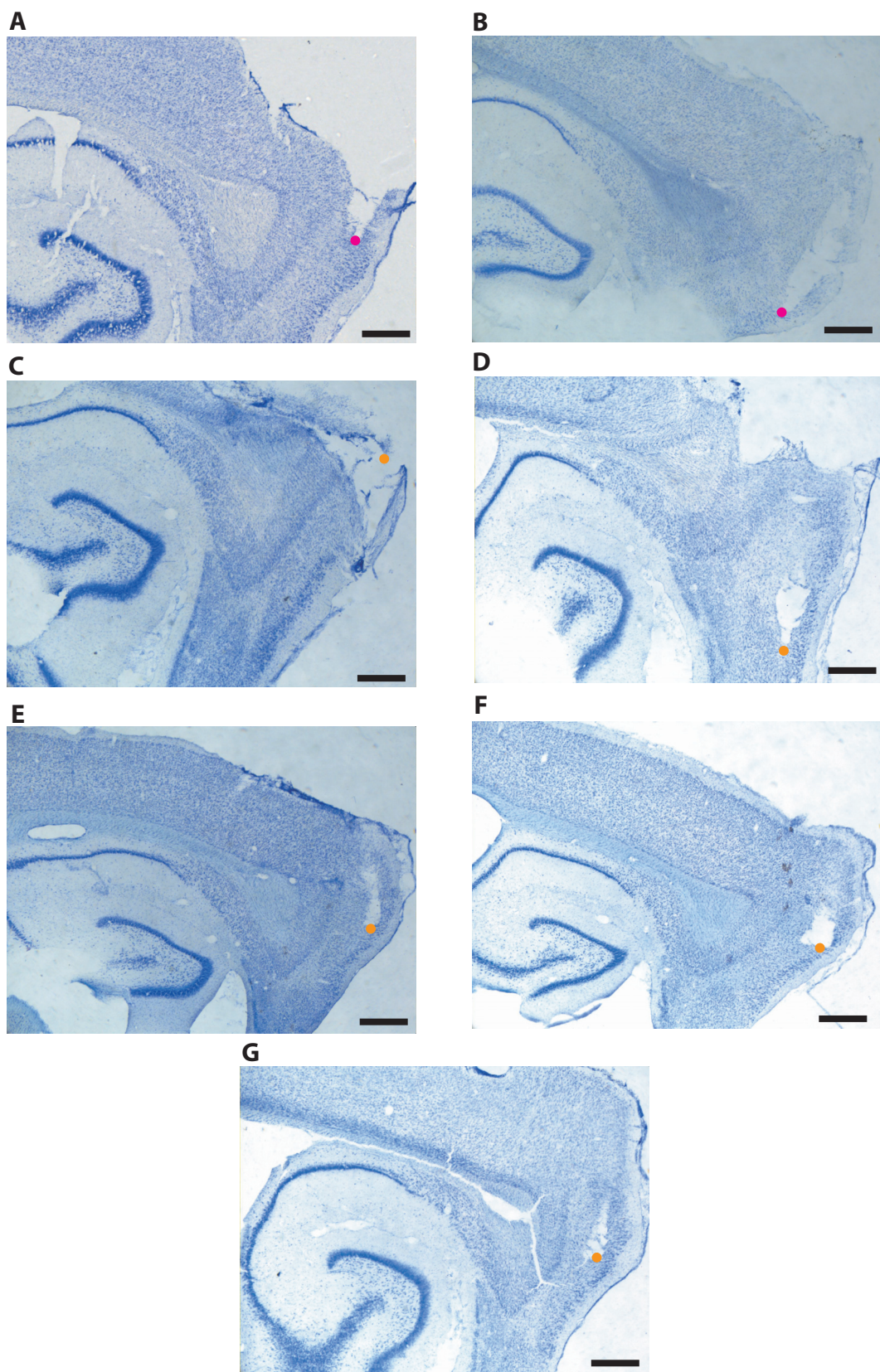


Fig. S1. Seven sagittal Nissl-stained brain sections showing the recording locations in superficial layers II-III in PaS, (A-B) magenta, and in mEC, (C-G) orange. Scale bar indicates 500 μ m. (A: r1682; B:r1738; C:r1728; D: r1709; E: r1737; F:r1739; G:r1710)

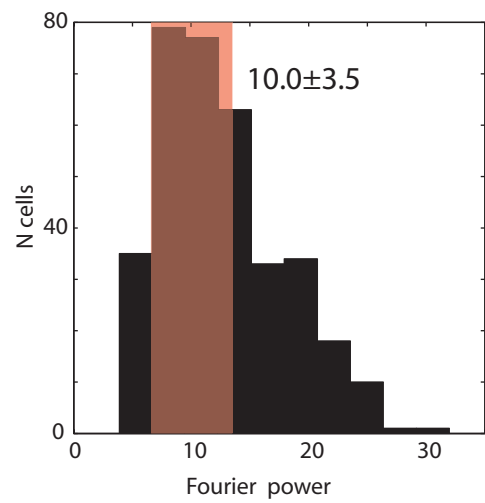
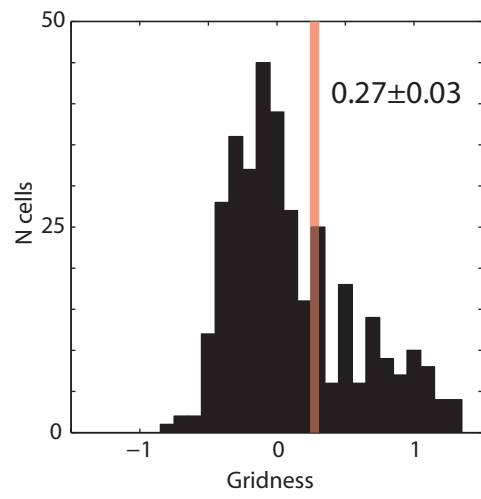
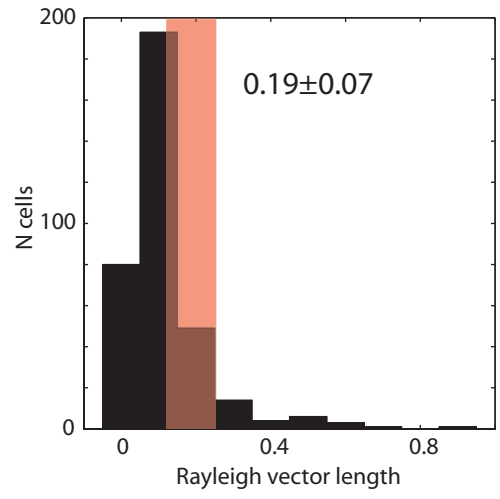
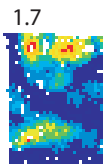
A**B****C**

Fig. S2. Frequency histograms of maximum normalised Fourier power (A), gridness (B), and Rayleigh vector length (C). Red bars represent the range of 95th percentile values from shuffled data. The range is defined as mean threshold \pm standard deviation.

r1682 021109d t1 c1



1.7

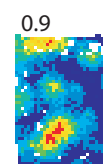
0.34

18.5

18.5



r1682 041109d t1 c3



0.9

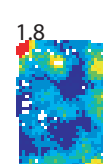
-0.12

16.7

16.7



r1682 091109c t1 c1



1.8

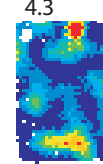
-0.22

10.7

10.7



r1682 131109c t1 c1



4.3

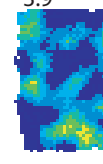
0.52

8.1

8.1



r1682 171109c t1 c1



3.9

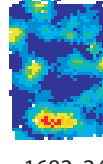
0.25

10.1

10.1



r1682 191109c t1 c1

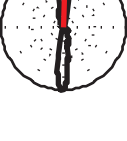


4.0

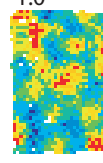
0.02

10.2

10.2



r1682 241109d t1 c3

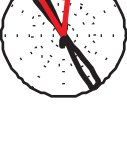


1.0

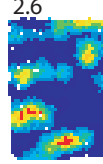
-0.06

7.6

7.6



r1682 251109c t1 c1

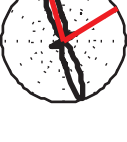


2.6

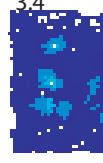
-0.16

18.2

18.2



r1682 271009b t2 c1

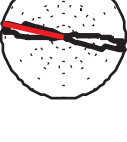


3.4

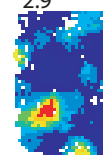
0.08

17.5

17.5



r1682 311009c t2 c1

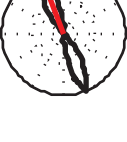


2.9

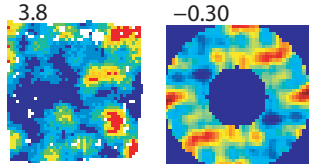
-0.40

13.7

13.7



r1682 041109d t2 c2



3.8

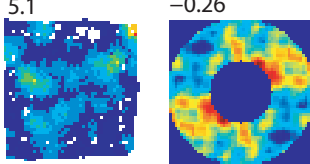
-0.30

8.1

8.1



r1682 041109d t2 c3

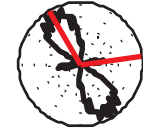


5.1

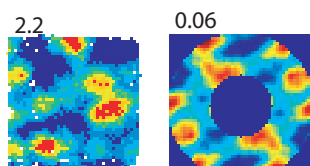
-0.26

8.5

8.5



r1682 061109c t2 c4



2.2

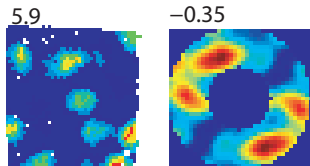
0.06

10.5

10.5



r1682 111109c t2 c1



5.9

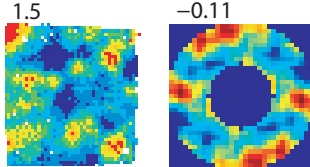
-0.35

12.6

12.6



r1682 111109c t2 c2

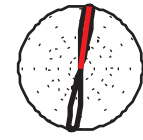


1.5

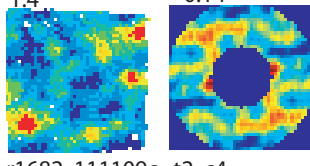
-0.11

8.7

8.7



r1682 111109c t2 c3



1.4

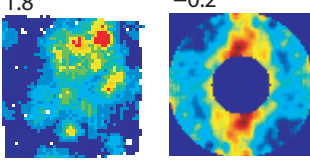
-0.14

9.6

9.6



r1682 111109c t2 c4

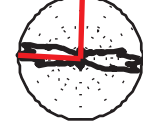


1.8

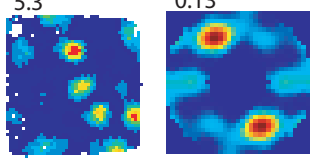
-0.2

12.0

12.0



r1682 131109c t2 c2

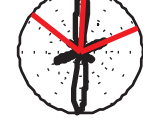


5.3

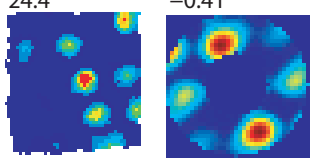
0.13

11.6

11.6



r1682 171109c t2 c1



24.4

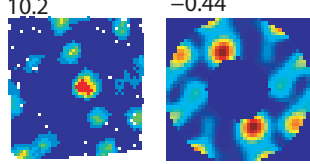
-0.41

15.0

15.0



r1682 251109c t2 c1



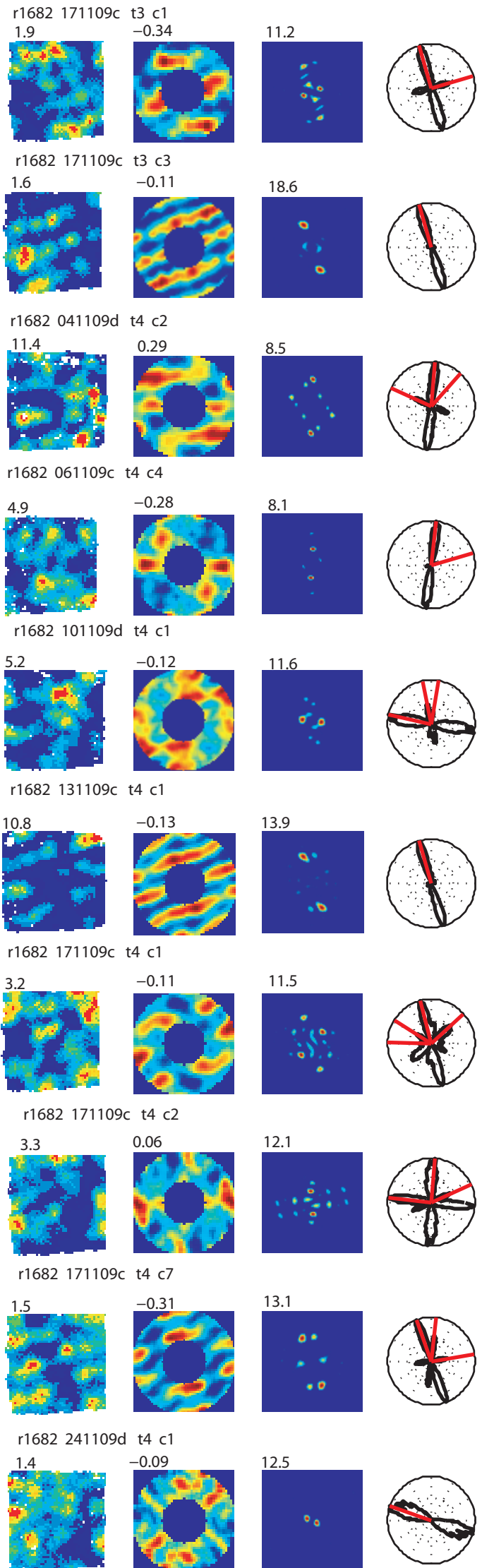
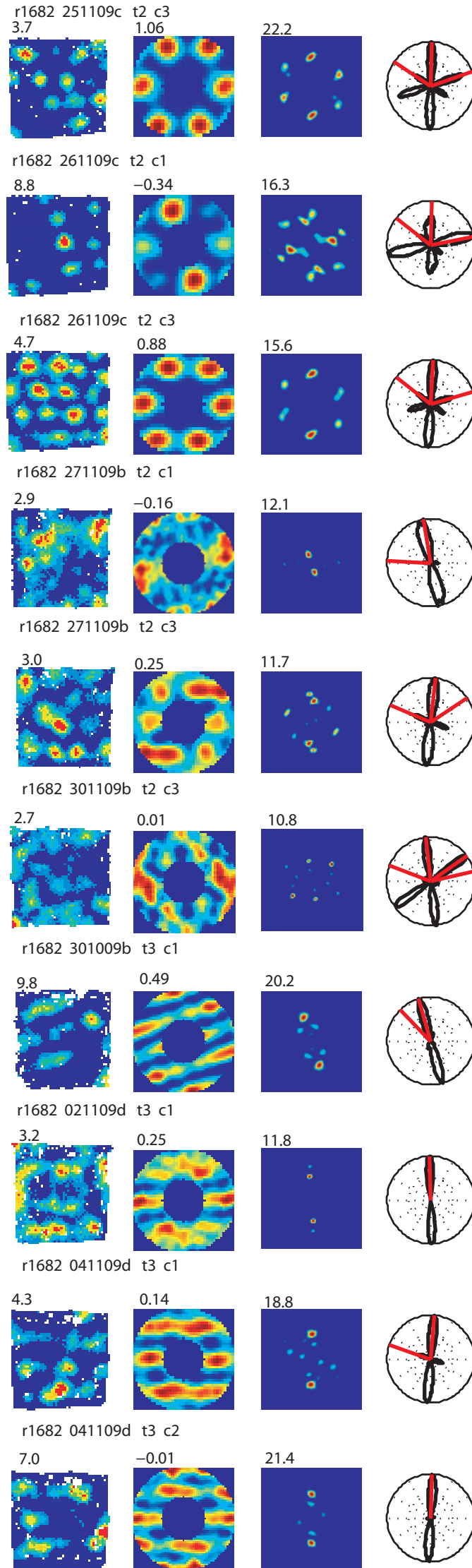
10.2

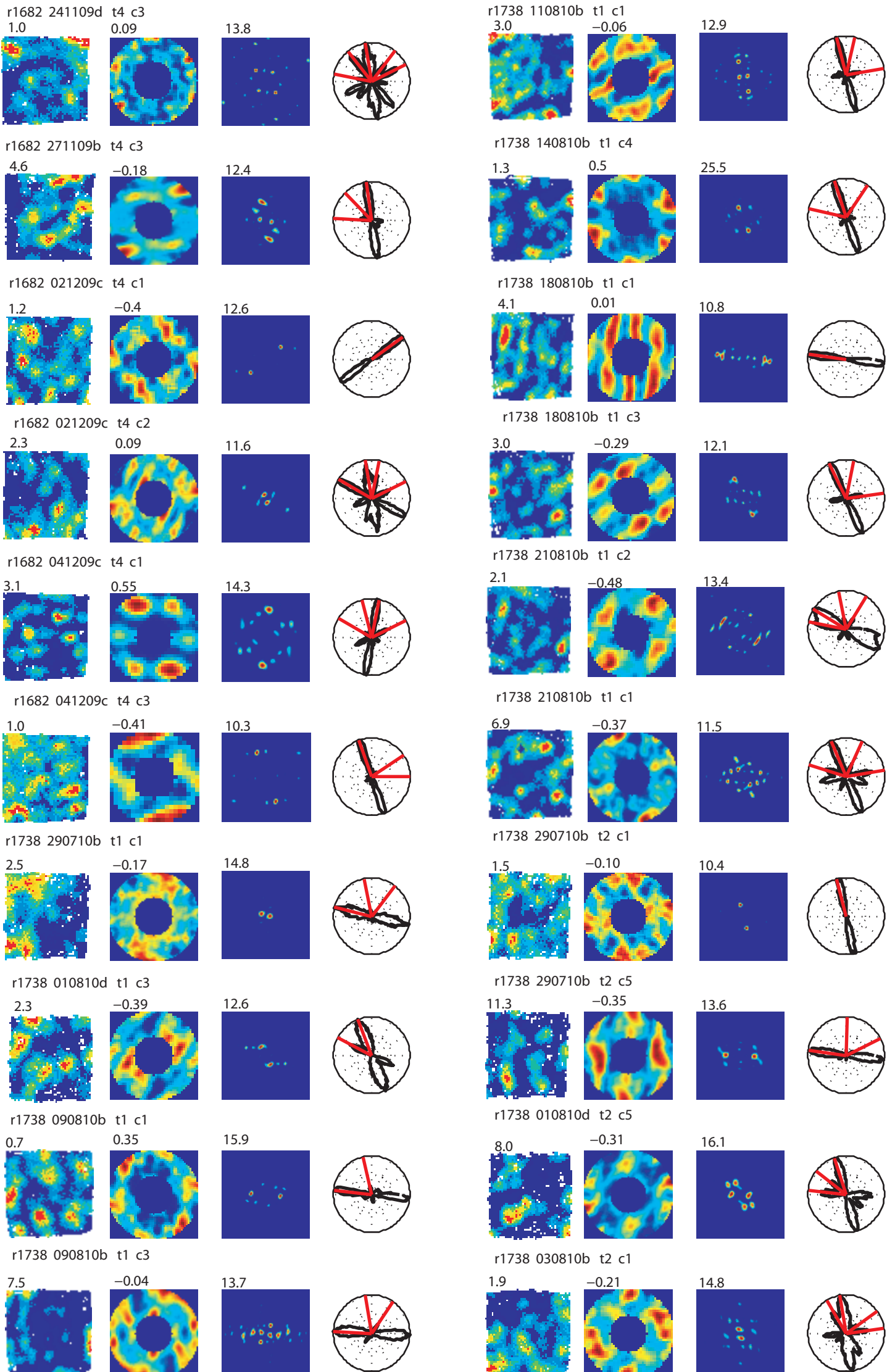
-0.44

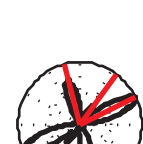
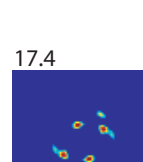
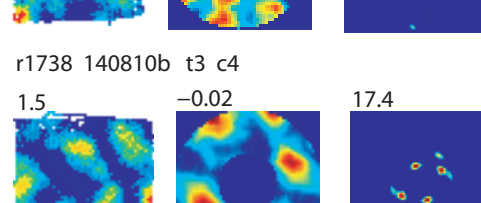
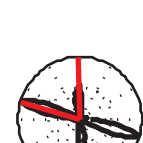
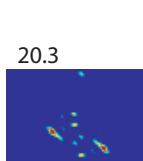
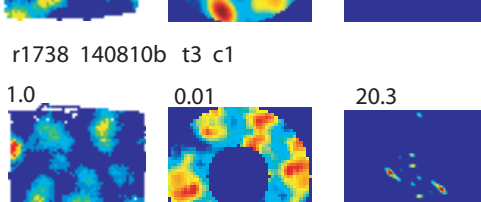
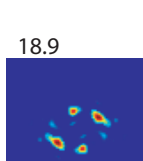
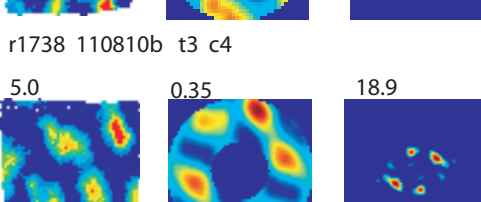
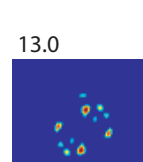
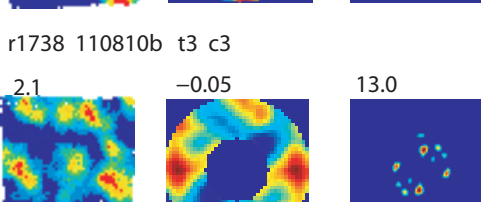
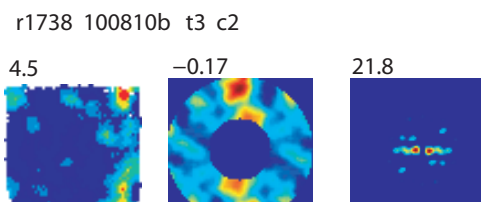
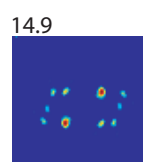
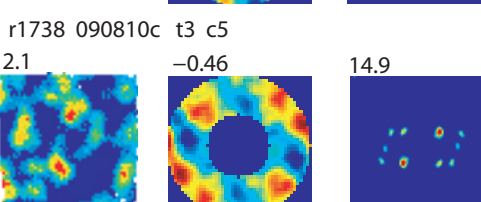
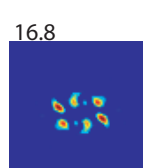
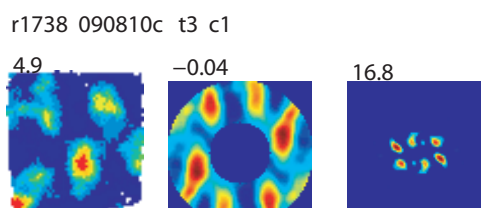
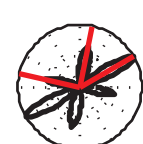
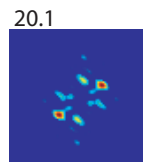
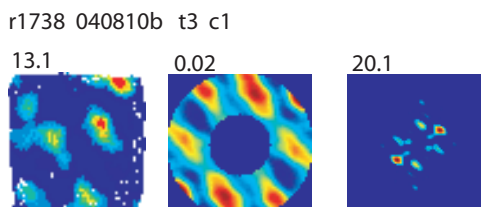
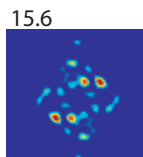
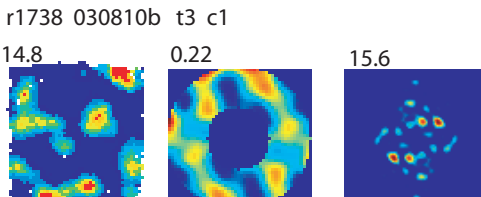
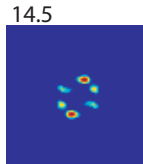
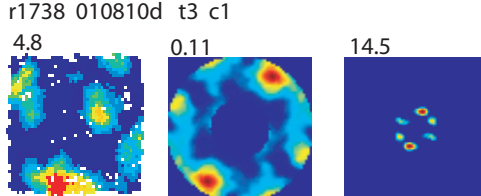
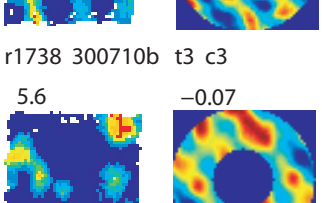
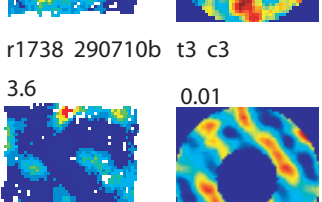
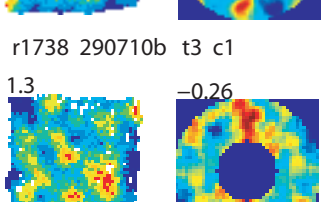
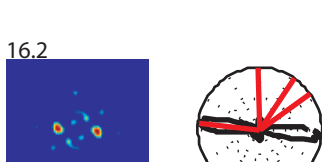
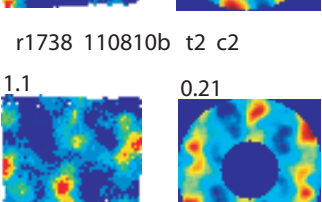
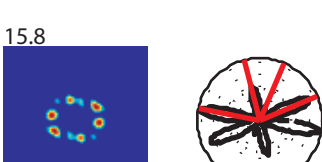
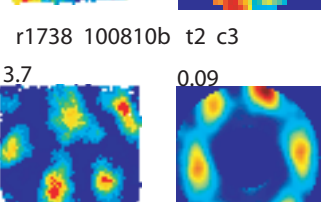
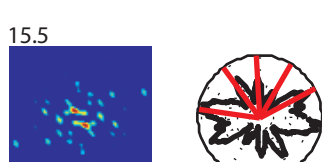
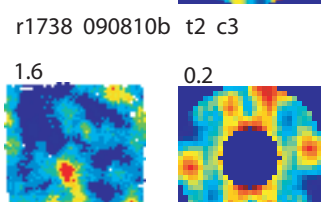
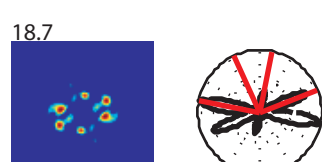
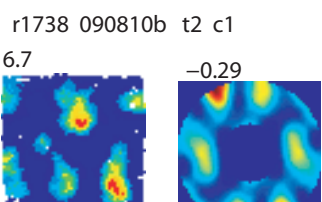
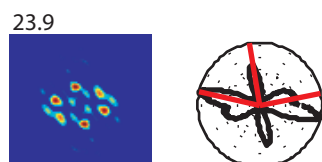
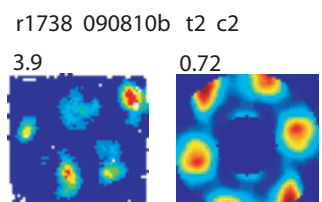
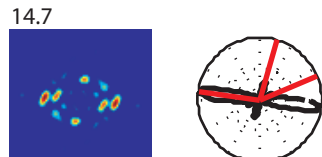
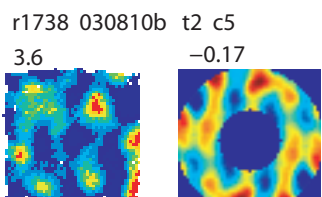
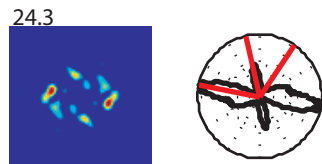
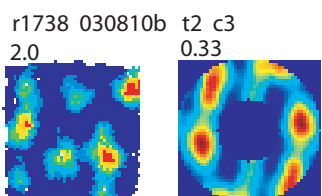
13.8

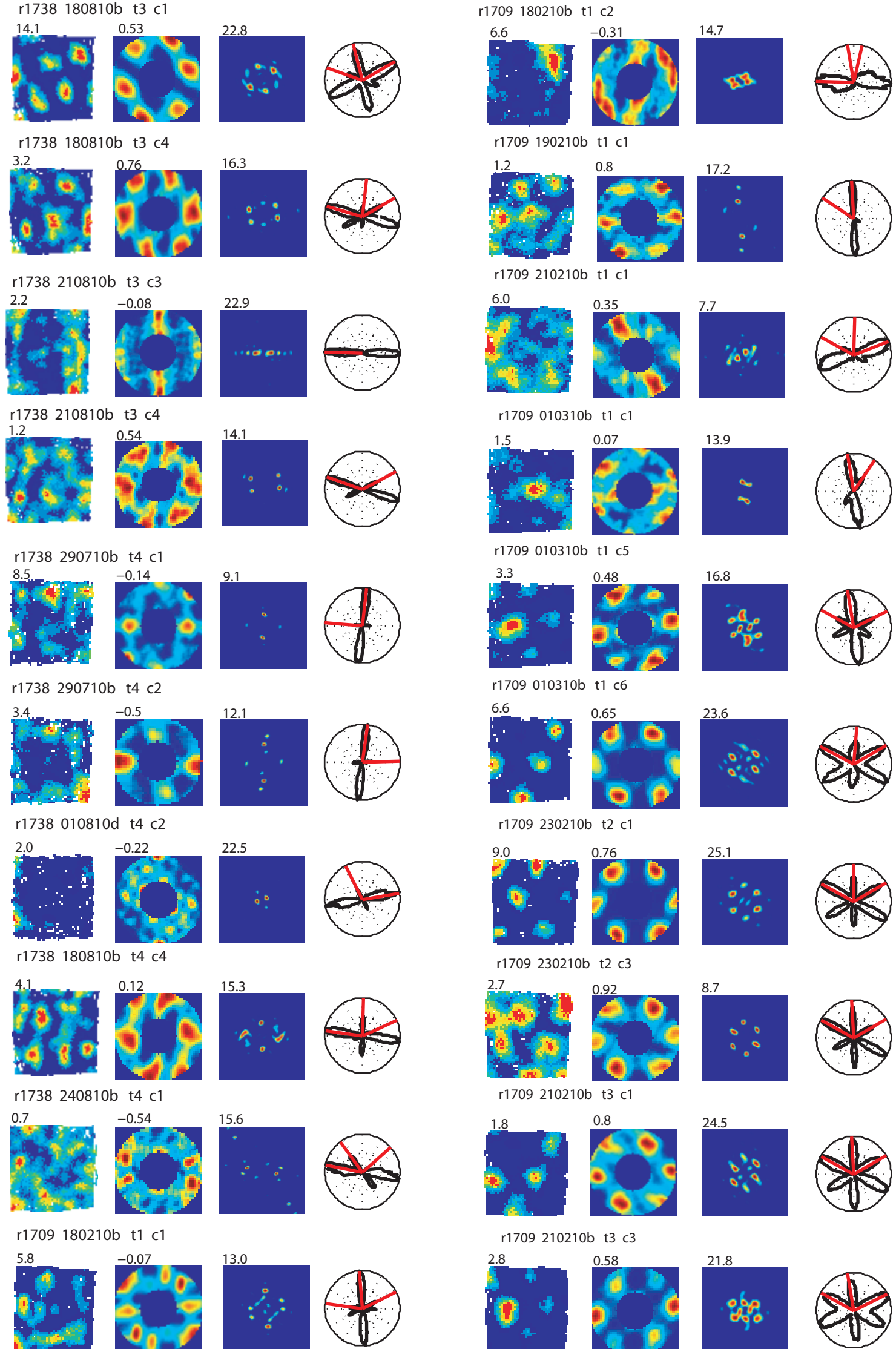
13.8

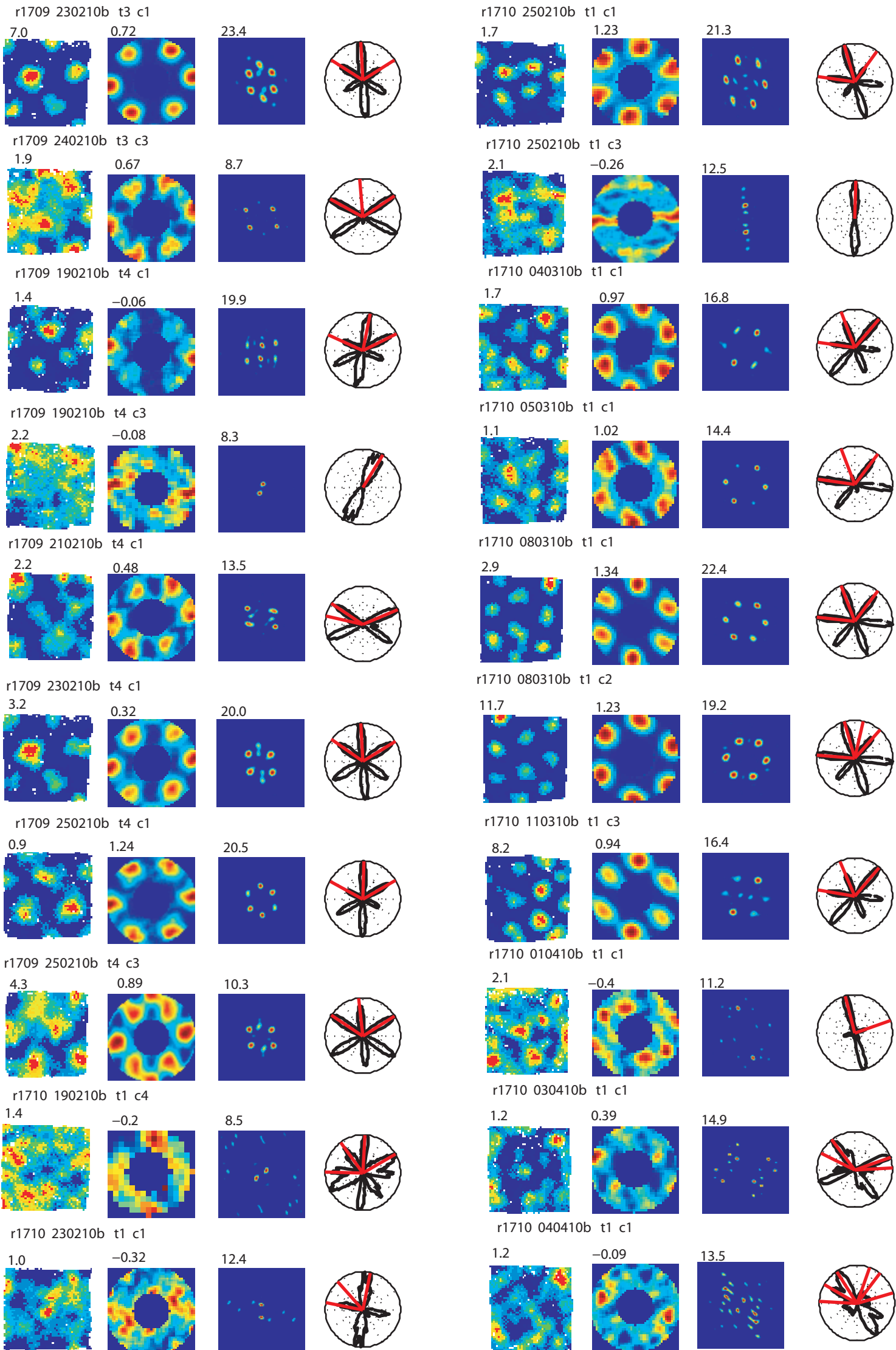


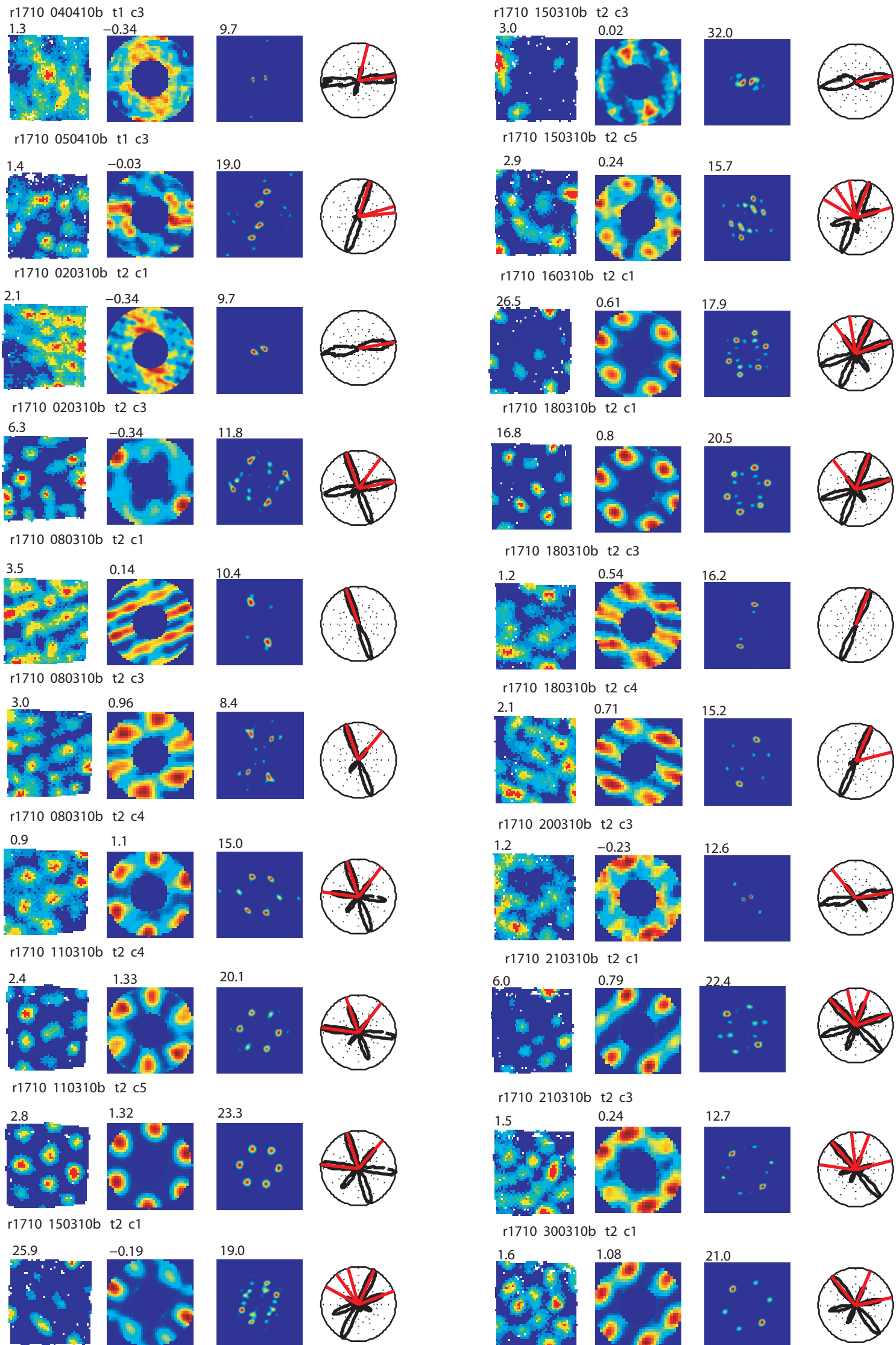


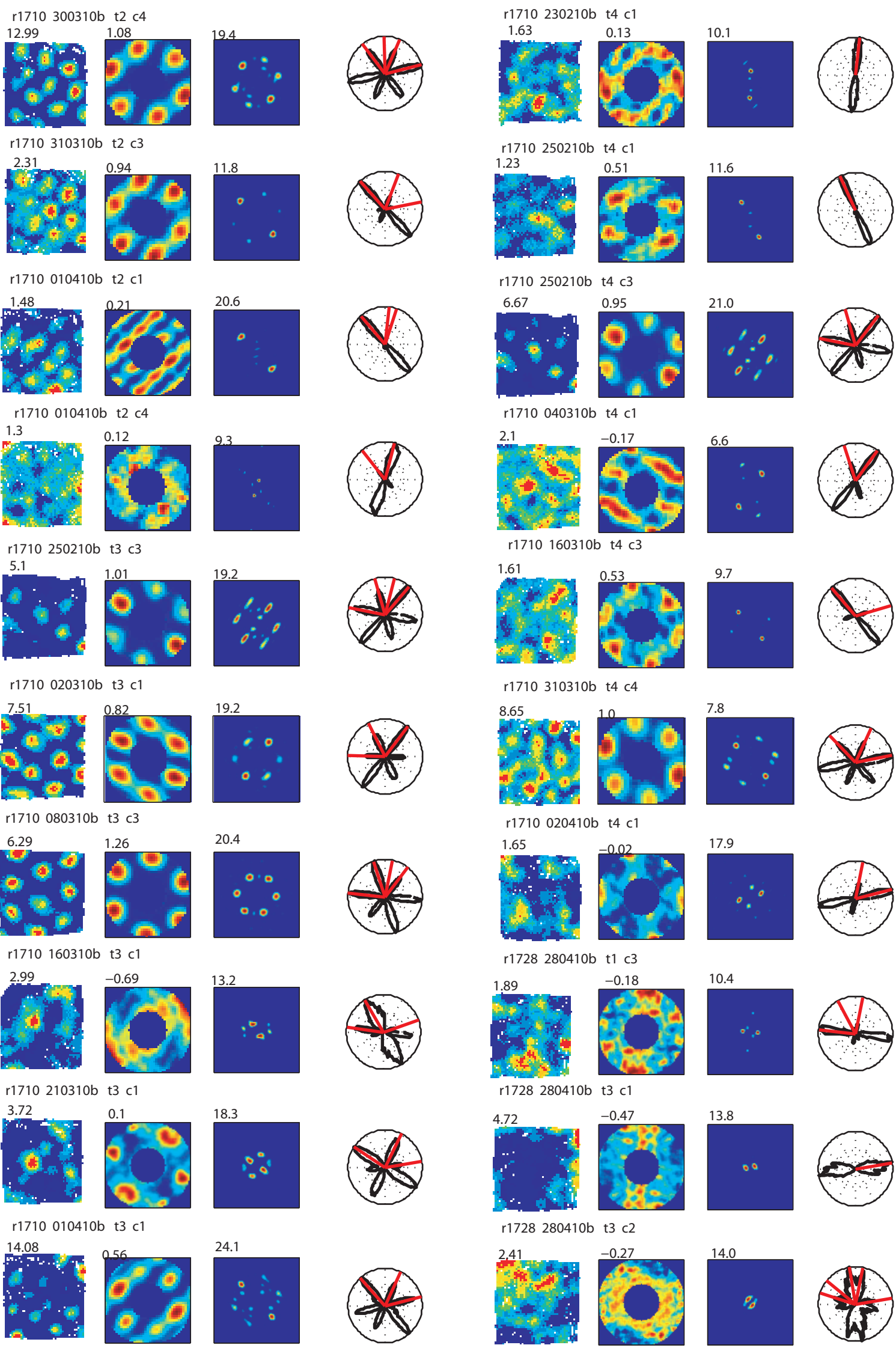


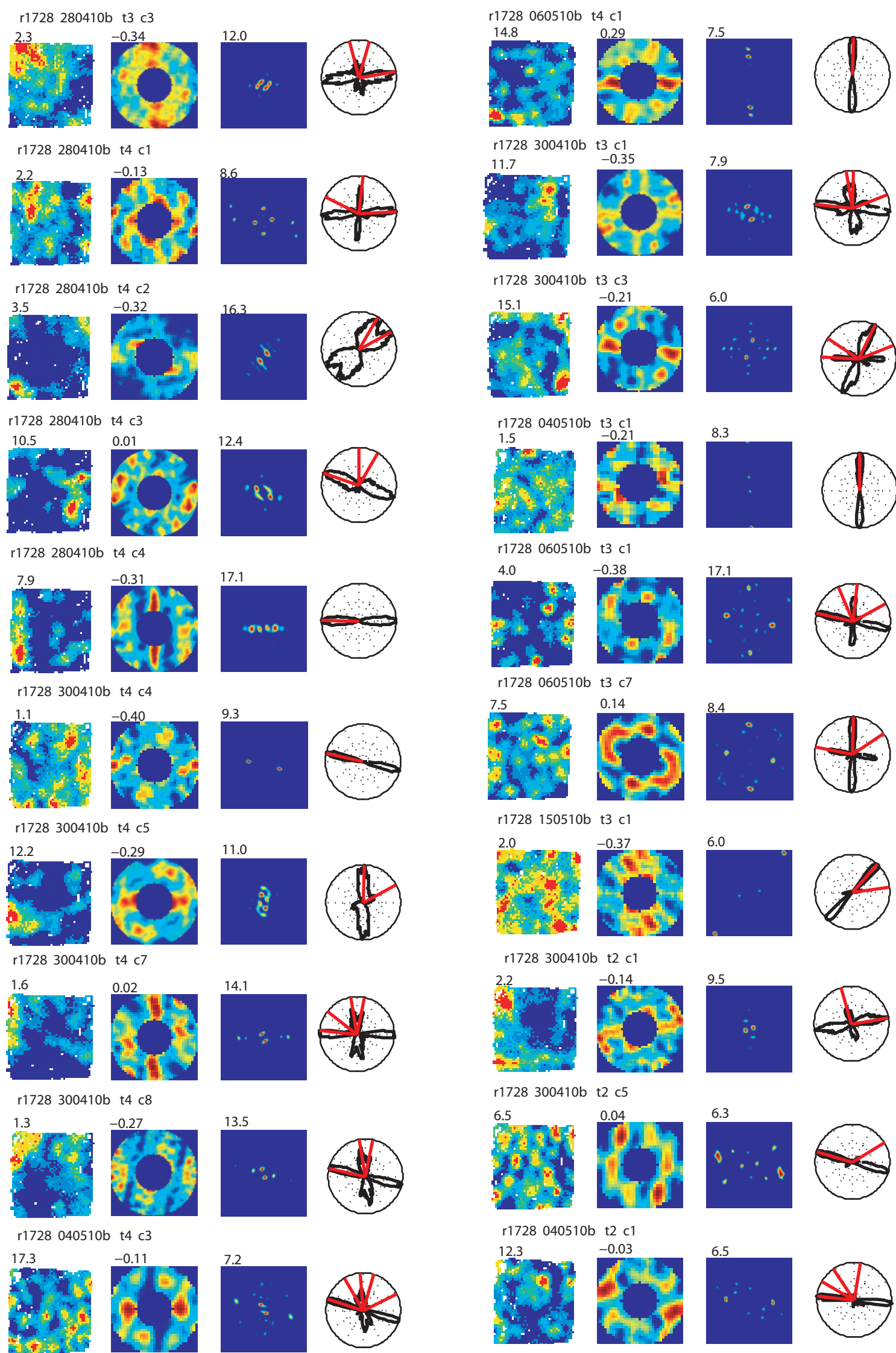


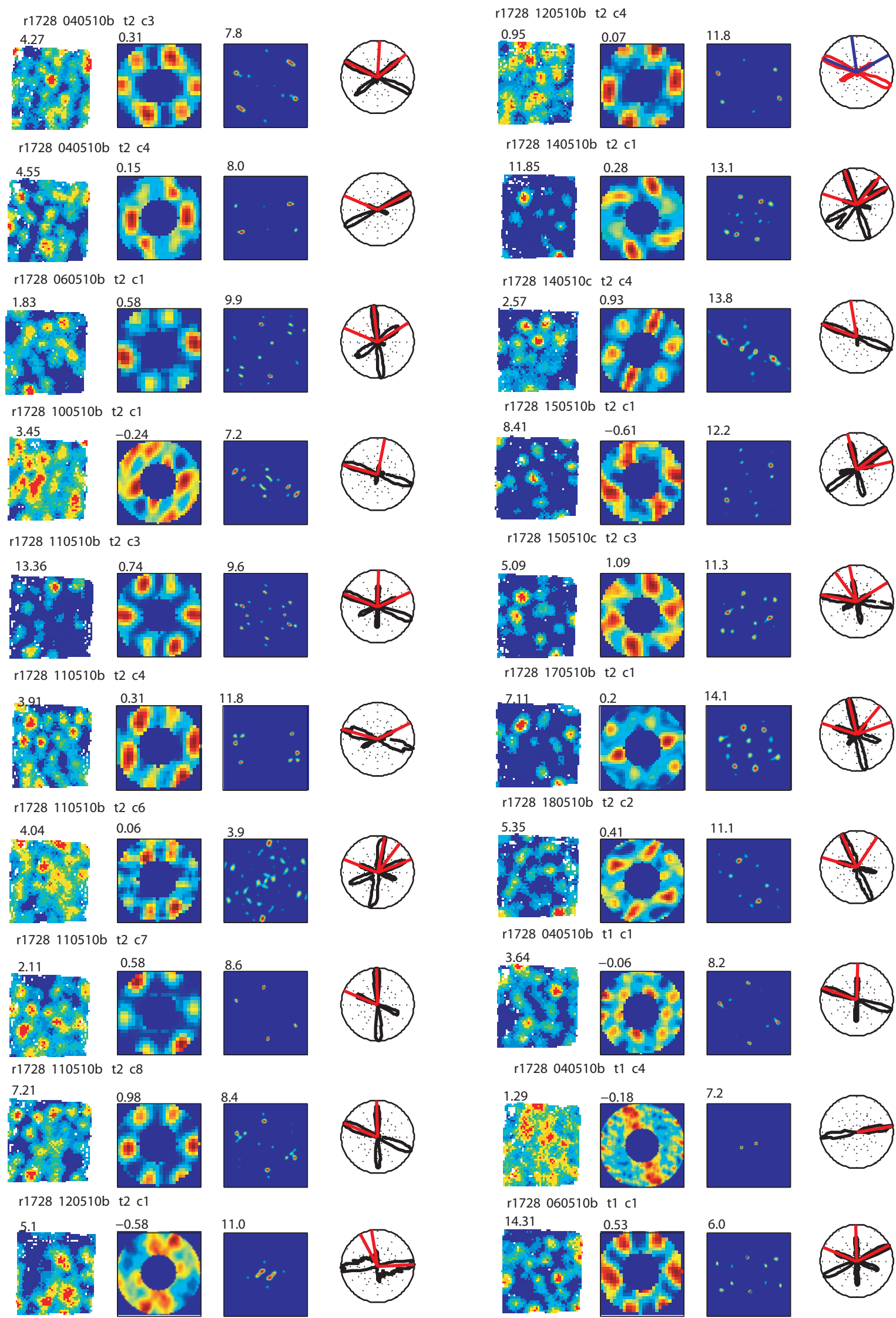


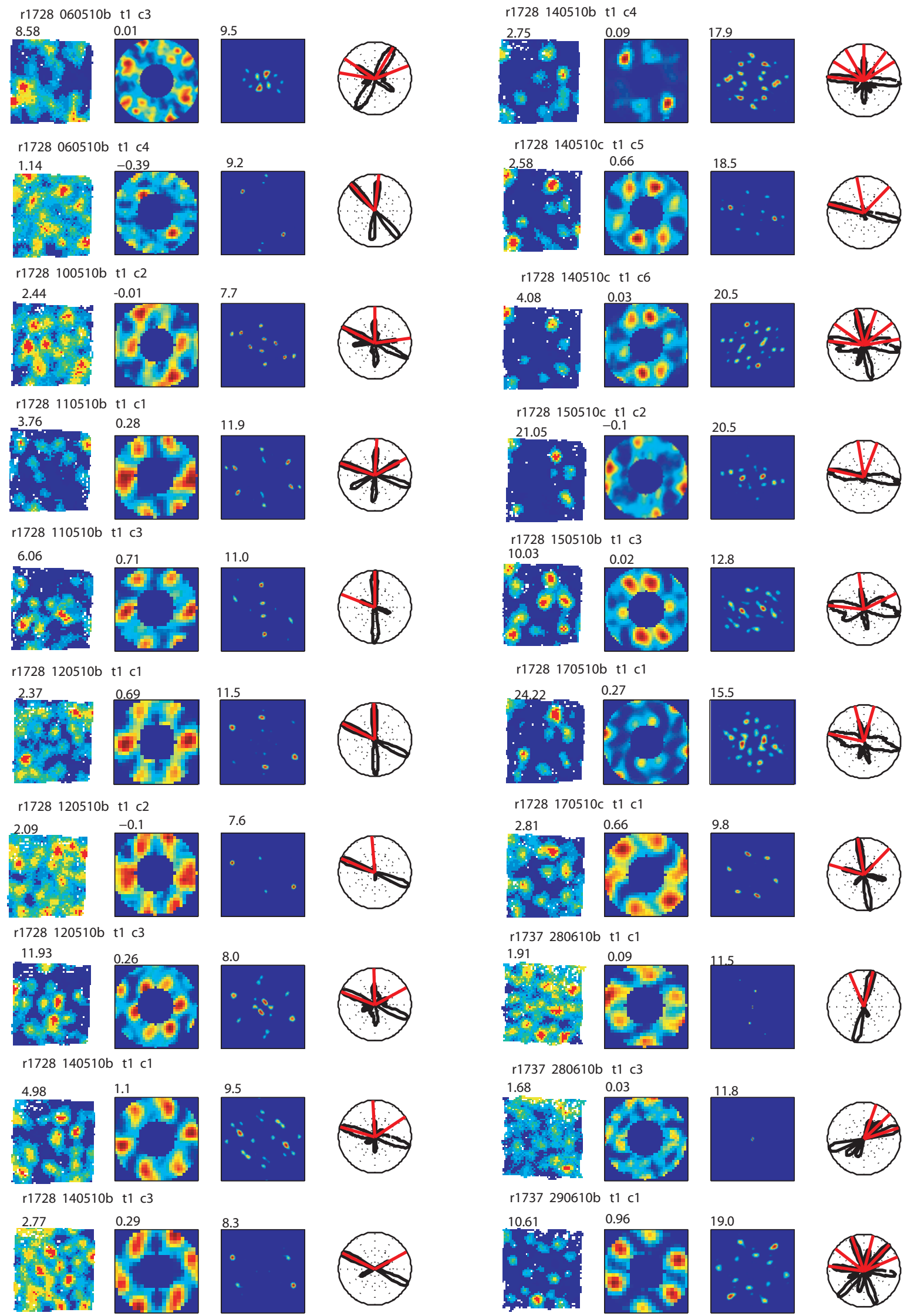




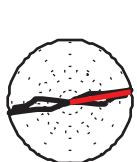
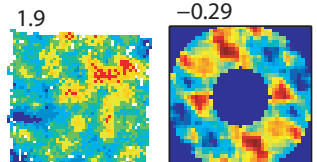




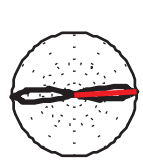
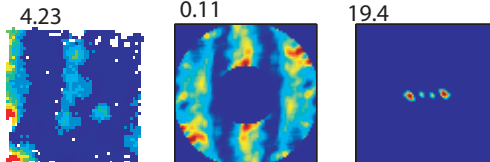




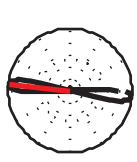
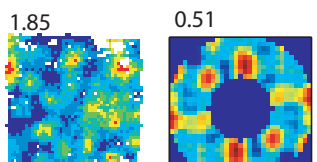
r1737 060710b t1 c4



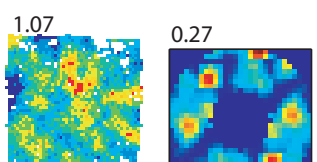
r1737 290610b t3 c1



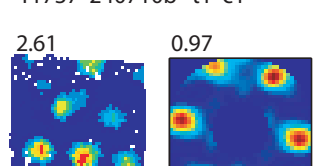
r1737 210710b t1 c3



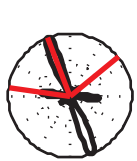
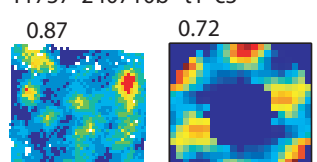
r1737 210710b t1 c4



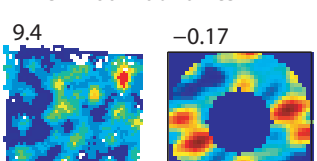
r1737 240710b t1 c1



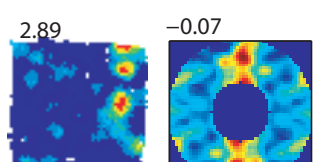
r1737 240710b t1 c3



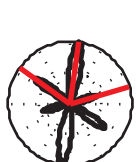
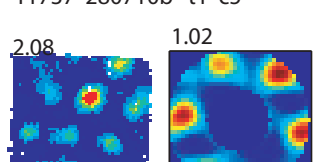
r1737 260710b t1 c3



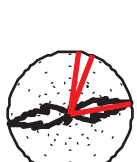
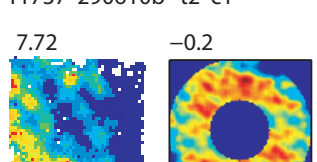
r1737 280710b t1 c3



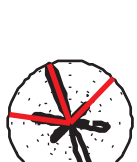
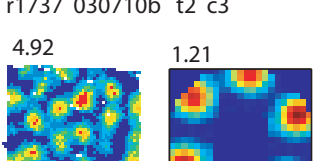
r1737 280710b t1 c5



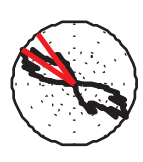
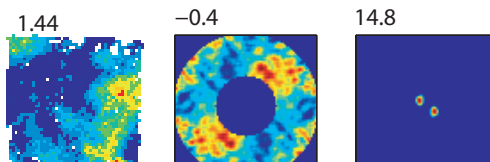
r1737 290610b t2 c1



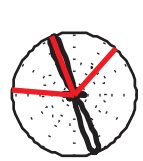
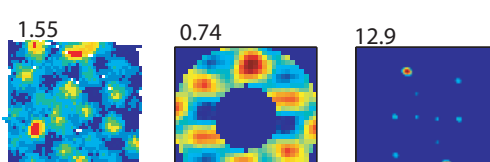
r1737 030710b t2 c3



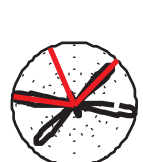
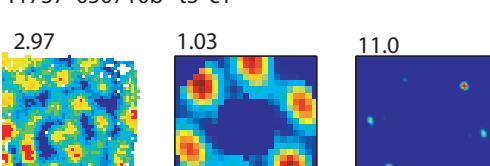
r1737 290610b t3 c3



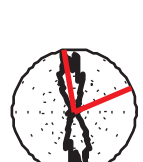
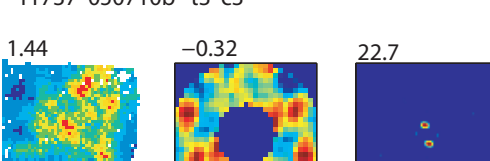
r1737 030710b t3 c3



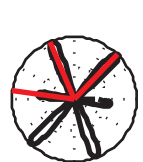
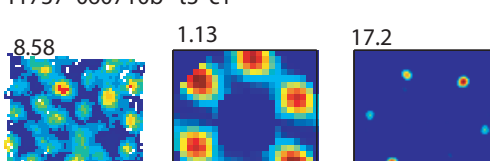
r1737 050710b t3 c1



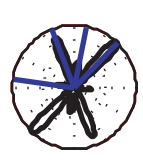
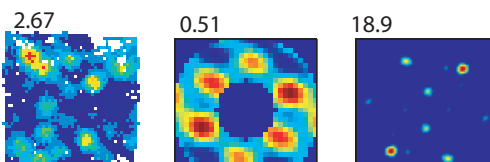
r1737 050710b t3 c3



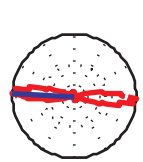
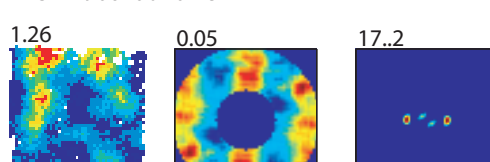
r1737 060710b t3 c1



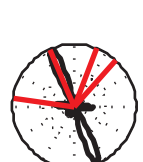
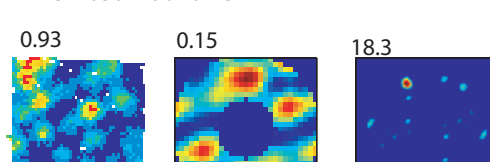
r1737 210710b t3 c3



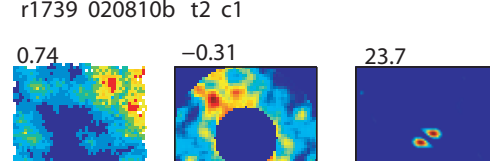
r1737 290610b t4 c1



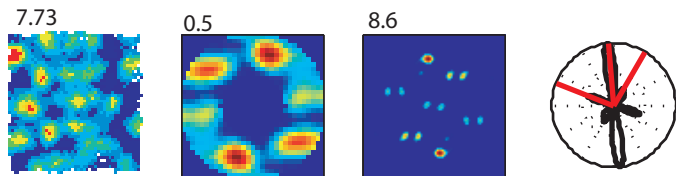
r1737 030710b t4 c1



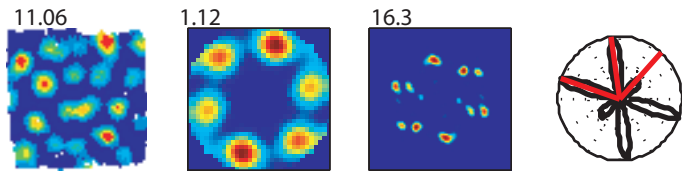
r1739 020810b t2 c1



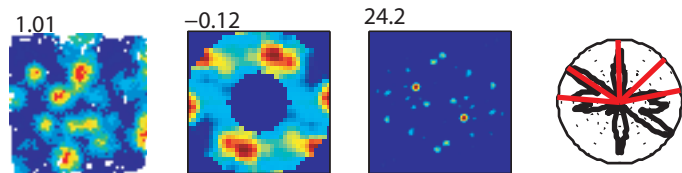
r1739 020810b t3 c1



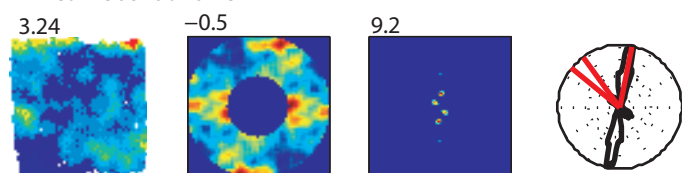
r1739 250810b t3 c1



r1739 270810b t3 c4



r1739 250810b t4 c4



r1739 250810b t4 c5

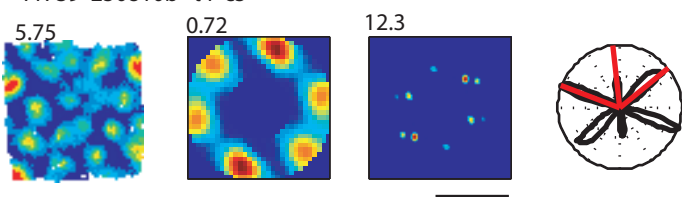


Fig. S3. The rate maps, spatial autocorrelograms, two dimensional Fourier spectrograms and Fourier polar plots of all the spatially periodic cells with their peak firing rate, gridness score and maximum Fourier power indicated on the top left corner of the rate maps, spatial autocorrelograms, two dimensional Fourier spectrograms respectively. Gridness was calculated by defining a mask on the spatial autocorrelogram centred on the central peak but excluding the peak itself bounded by a circle defined by the mean distance from the centre to the closest peaks multiplied by 2.5. This area was rotated in 30 degrees increments up to 150 degrees and for each rotation the Pearson product-moment correlation coefficient was calculated against the un-rotated mask.

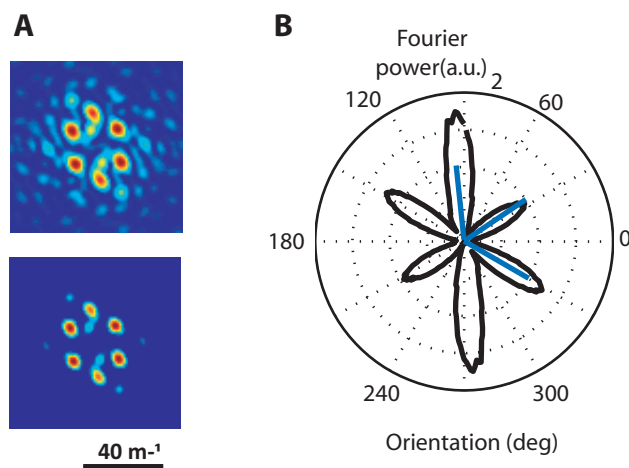


Fig. S4. Estimating significant Fourier components from Fourier polar plots. (A) A typical 2D Fourier spectrogram of a grid cell before subtraction of 50th percentile value from shuffled data (top) and after (bottom). (B) Fourier polar plot calculated from the ‘cleaned’ two dimensional Fourier spectrogram in (A, bottom); values smaller than 10% of the maximum power of the Fourier polar plot were removed to avoid counting sub-harmonics. Orientations of the significant Fourier components are shown in blue.

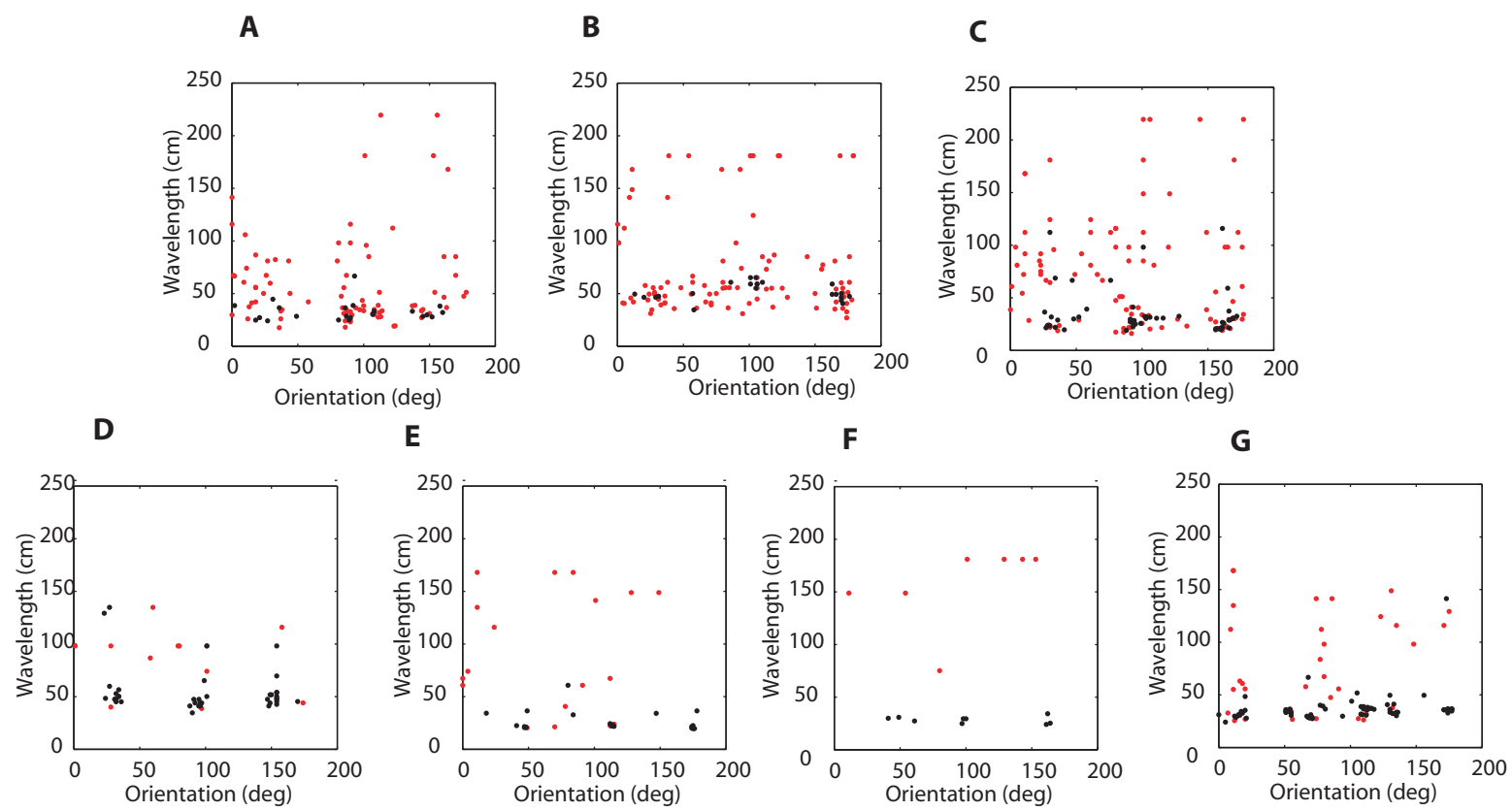


Fig. S5. The distributions of wavelengths and orientations of significant Fourier components. (A-B) cells from PaS; (C-G) cells from mEC. ((A): r1682; (B) : r1738; (C): r1728; (D): r1709; (E): r1737; (F):r1739; (G): r1710). Grid cells shown in black, other spatially periodic (non-grid) cells shown in red.

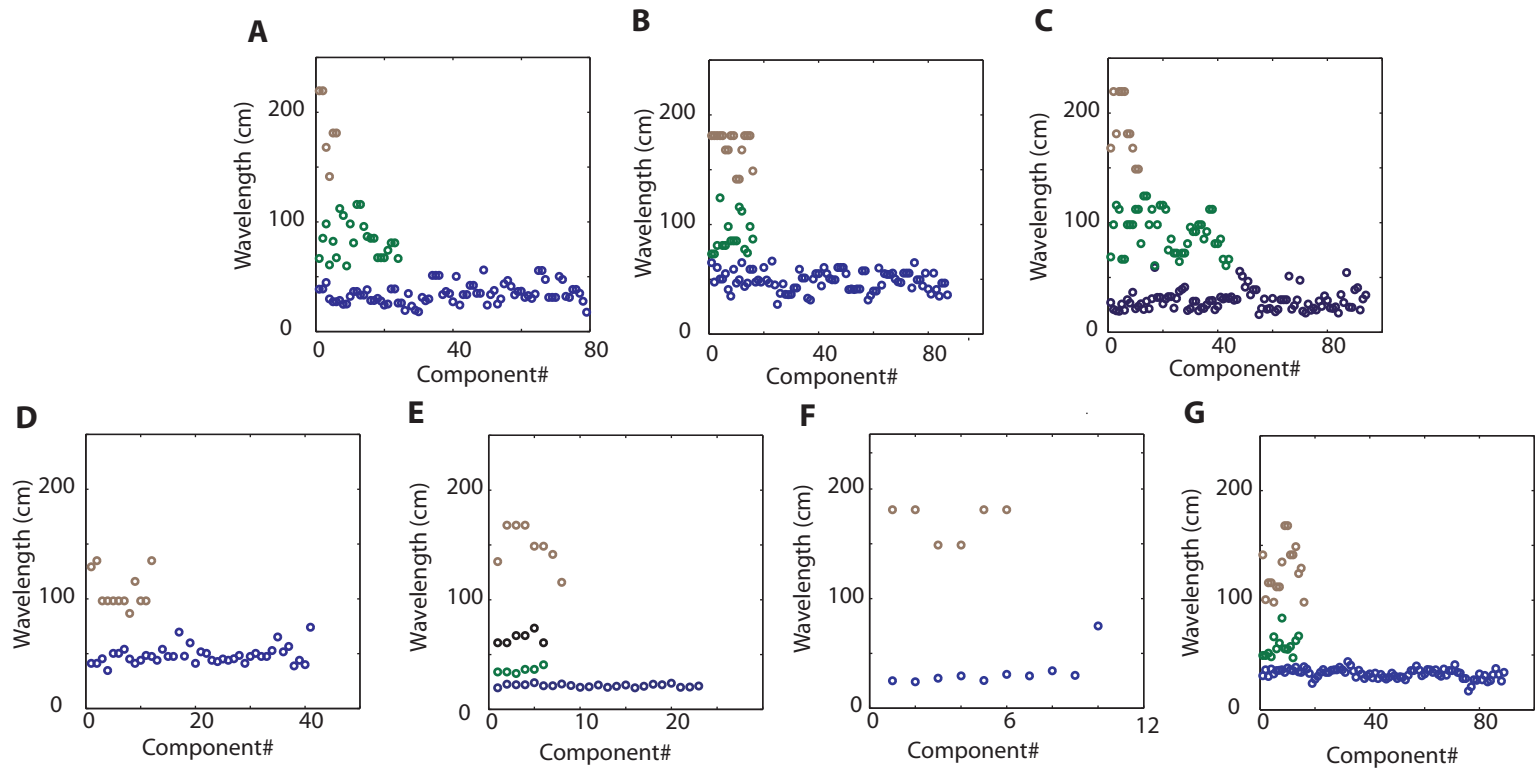


Fig. S6. The clustering of wavelengths of significant Fourier components. Different colors mark distinct clusters. Brown clusters corresponding to the larger wavelengths (with mean wavelength >100 cm) were not included into the analysis. (A-B) cells in PaS; (C-G) cells in mEC (A: r1682; B: r1738; C: r1728; D: r1709; E: r1737; F: r1739; G: r1710). All clusters were significantly more clustered than expected by chance ($P < 0.05$). Namely, A: blue: 34.4 ± 8.9 (<17.5), green: 83.6 ± 17.3 (<19.4); B: blue: 48.6 ± 9.1 (17.7); green: 89.5 ± 15.9 (16.5); C: blue: 28.9 ± 9.0 (<19.8); green: 91.0 ± 18.8 (<20.2); D: blue: 48.4 ± 7.9 (<14.3); E: blue: 21.7 ± 1.3 (<8.6); green: 35.9 ± 2.8 (<10.6); black: 65.2 ± 5.4 (10.9); F: blue: 33.1 ± 15.1 (<18.0); G: blue: 33.0 ± 4.5 (<13.6); green: 58.0 ± 9.8 (<14.1), here the mean \pm sd of the data was specified (and compared to the 95th percentile of sd of the data surrogate).

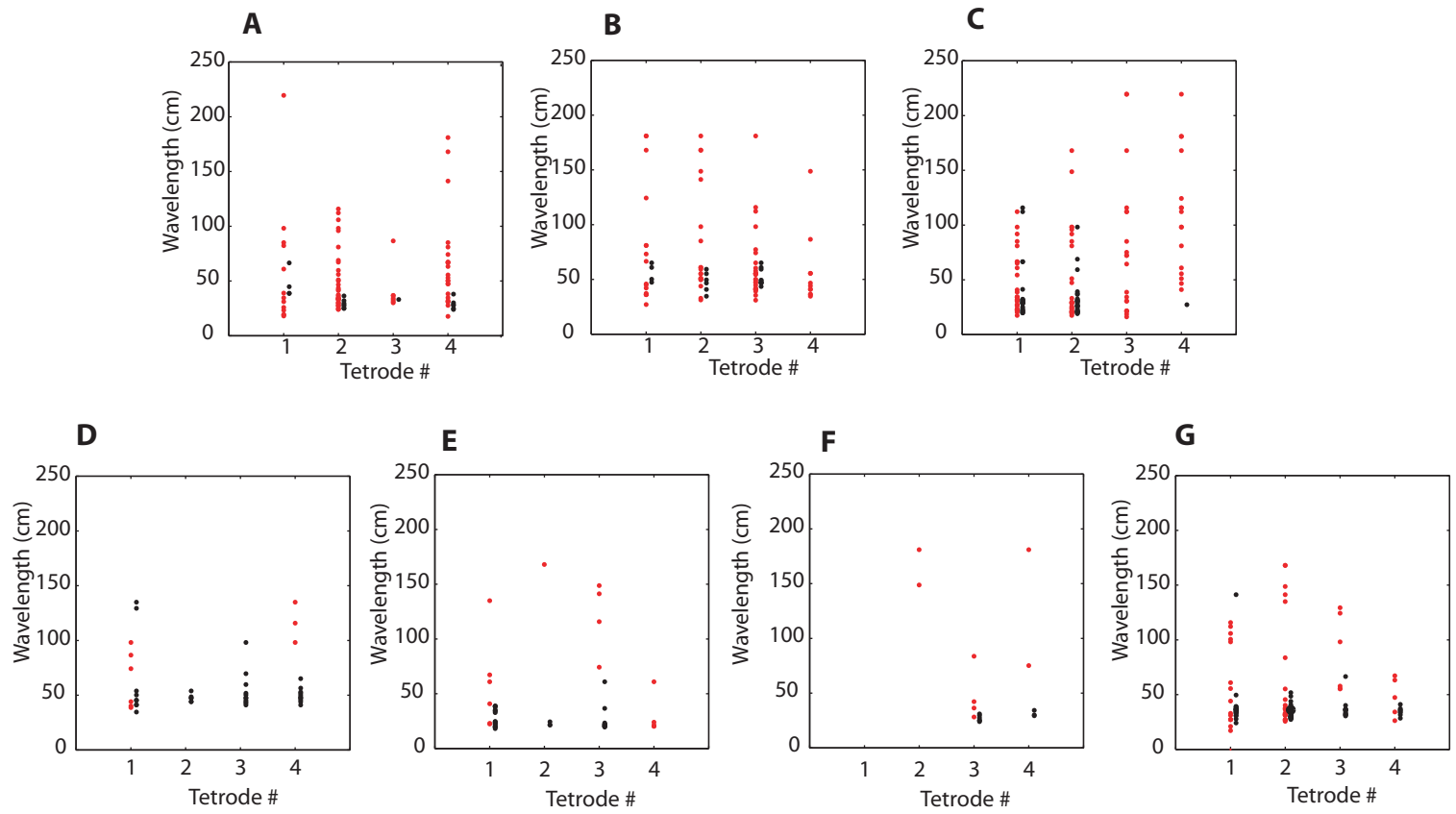


Fig. S7. The distributions of wavelengths of significant Fourier components for each tetrode in each animal. (A-B) cells from PaS; (C-G) cells from mEC. ((A): r1682; (B) : r1738; (C): r1728; (D): r1709; (E): r1737; (F):r1739; (G): r1710). Grid cells shown in black, other spatially periodic (non-grid) cells shown in red.

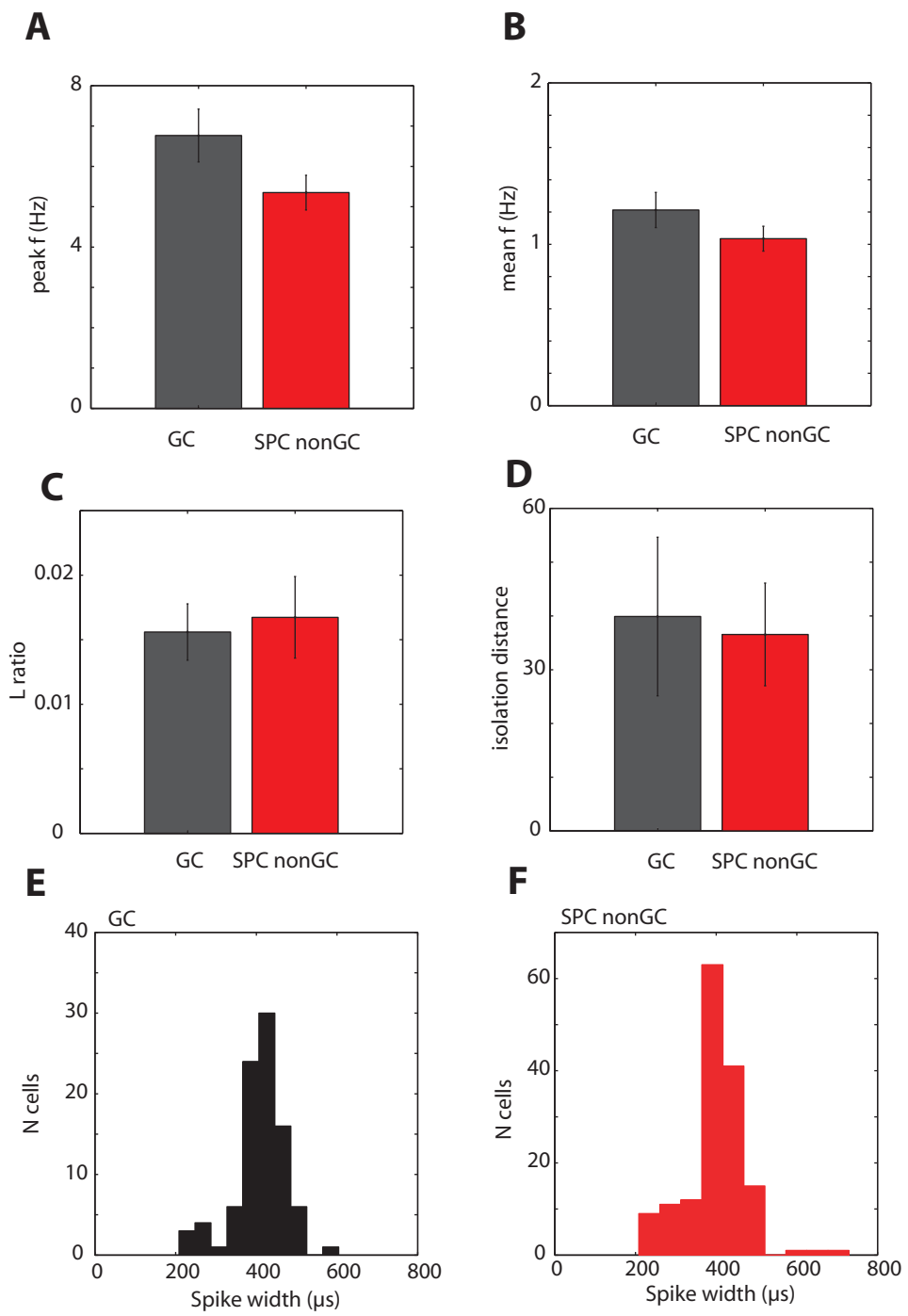


Fig. S8. Firing properties and cluster quality of spatially periodic non-grid cells (red) are comparable to grid cells (black), $P>0.05$. (A-B) Peak, a, and mean, b, firing rates averaged across all the rats. (C-D), L ratio, (C), and isolation distance, (D), averaged across all the rats. (E-F) Distribution of spike width (peak-trough) of grid cells and other spatially periodic cells. The average spike width is around 400 μ s independent of the recording site.

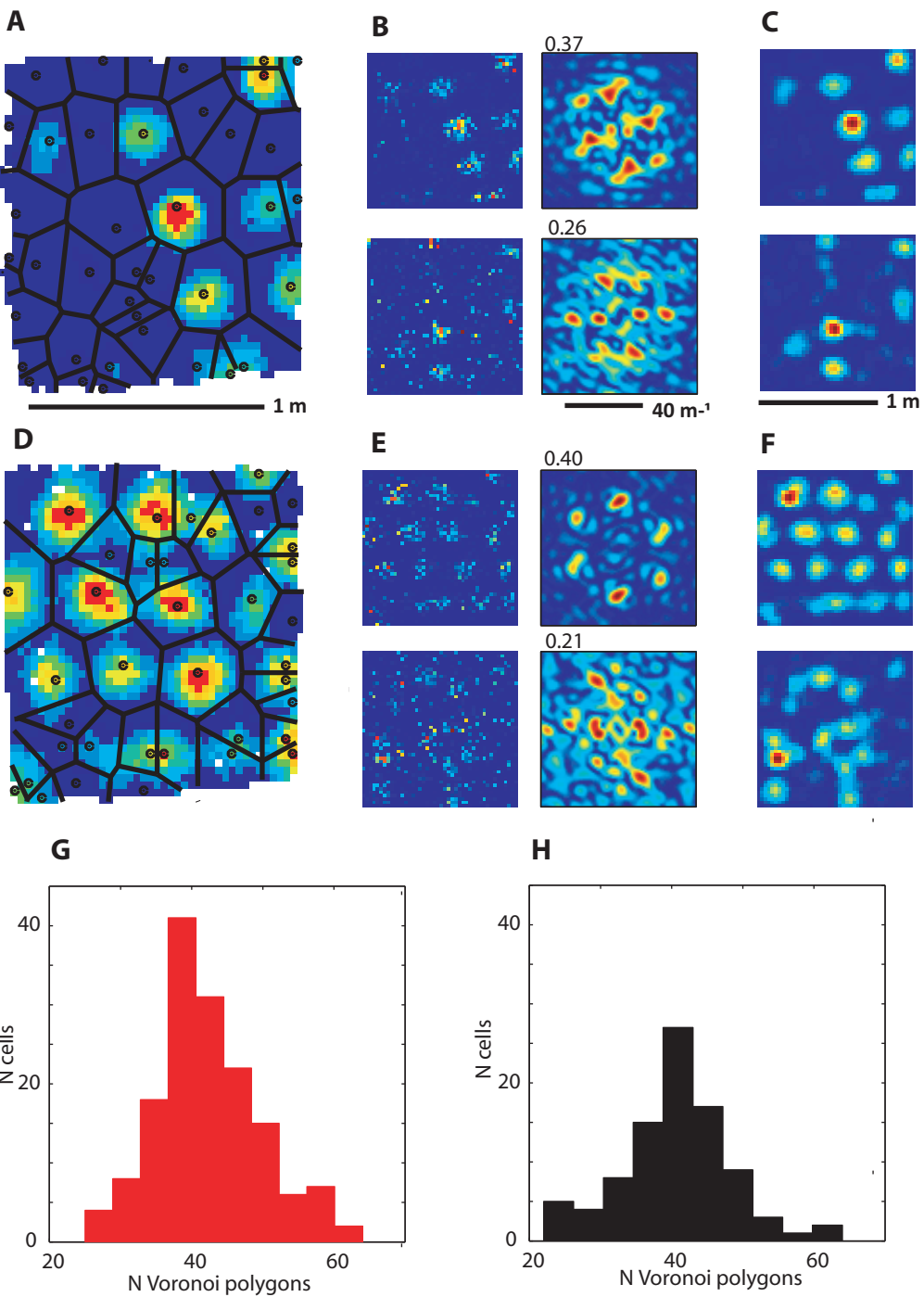


Fig. S9. Spatial shuffling preserving local spatial structure. (A) A spatially periodic non-grid cell firing rate map (with adaptive smoothing), showing all local maxima (dots) and the Voronoi polygons centred on them (lines). (B) The unsmoothed ratemap (left) and resulting 2D Fourier spectrogram (right) of the cell (above) and a shuffled surrogate corresponding to random re-positioning of the Voronoi polygons (below). (C) Smoothed ratemaps for the cell (above) and the surrogate (below) for comparison (both using the same Gaussian smoothing kernel). (D-F) Similar figures to (A-C), showing a grid cell and a shuffled surrogate. Numbers above spectrograms show the measure of peak Fourier power. Note that these differ in magnitude from those in Figs 1&3 due to differences in the normalization techniques used. (G-H) Distribution of the number of Voronoi polygons found for spatially periodic non-grid cells (G, red) and grid cells (H, black).

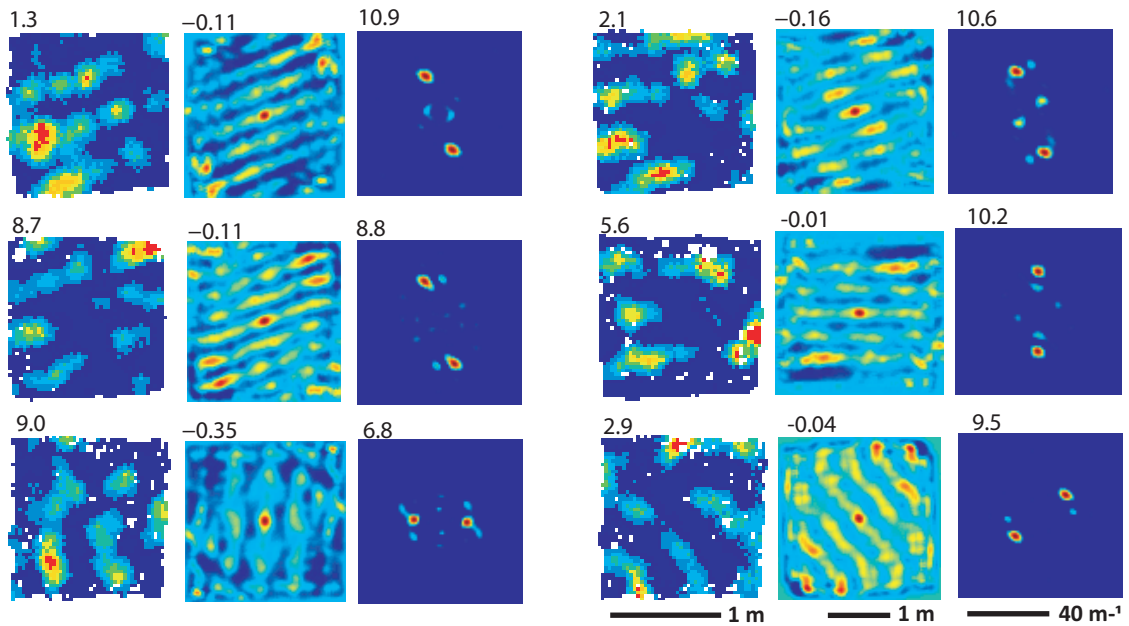
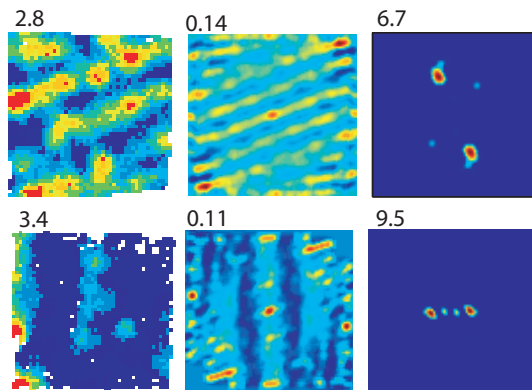
A**B**

Fig. S10. Examples of band-like cells in PaS, (A), and in mEC, (B). The rate map (1.3 m square enclosure), spatial autocorrelogram and 2D Fourier spectrogram with peak firing rate, gridness and maximum Fourier power (top left) are shown for each cell.

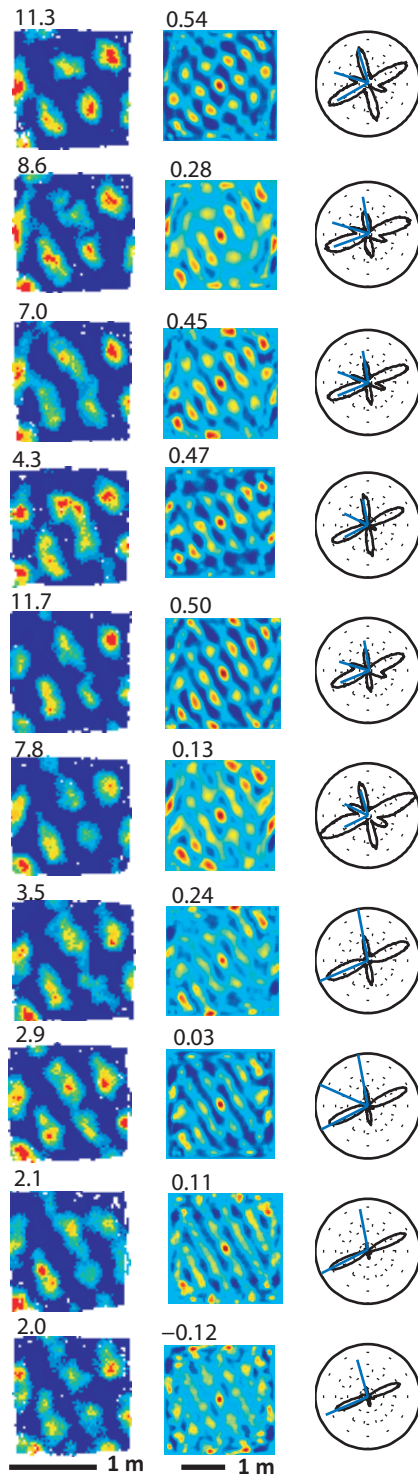


Fig. S11. Ten trials of the same spatially periodic cell recorded across five days. Rate maps with the peak firing rates, left, spatial autocorrelograms with the gridness score, middle, and Fourier polar plots, right, are shown. The significant Fourier components are indicated in blue.

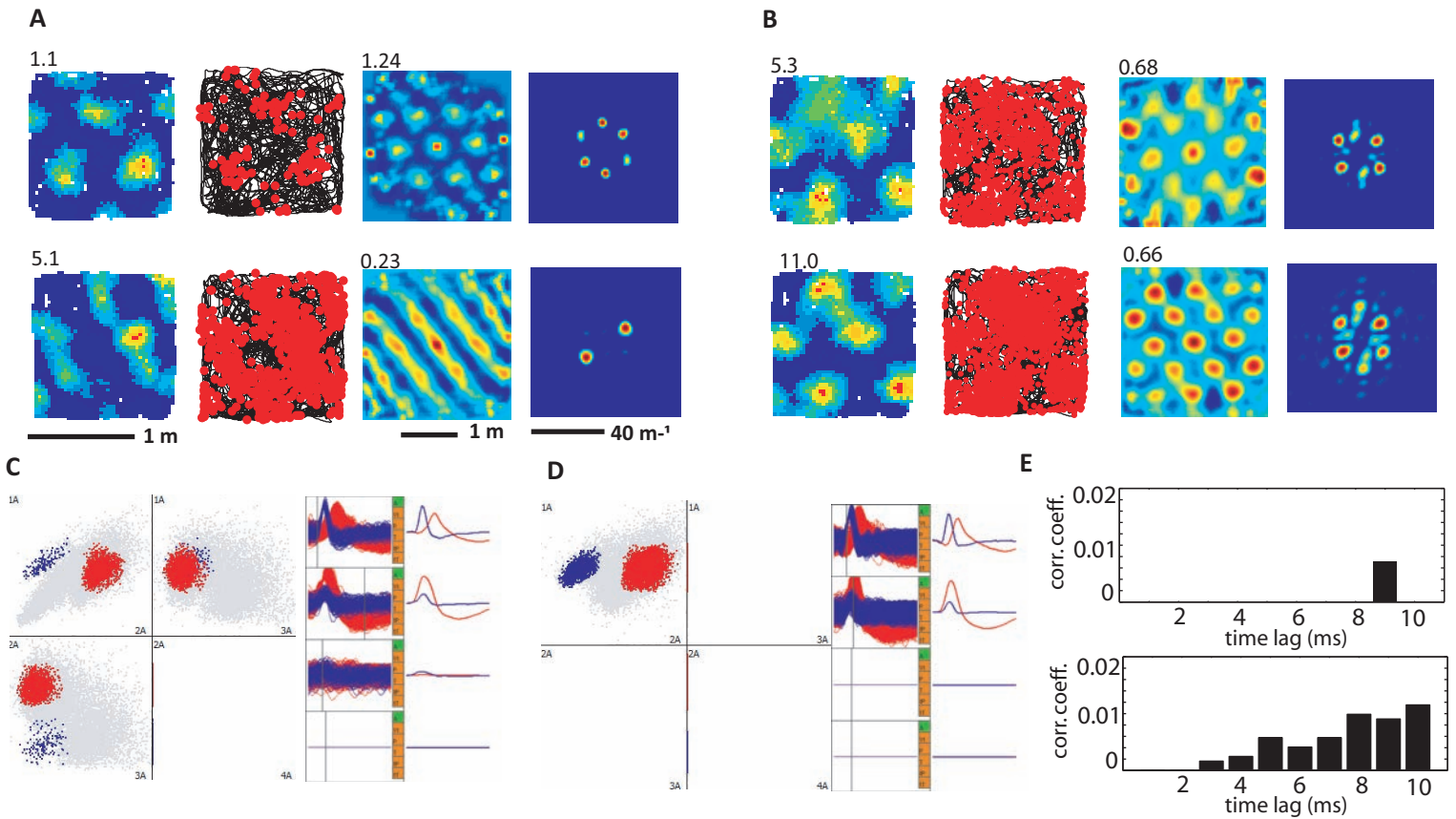


Fig. S12. Grid cell changing into a band-like cell. (A) Rate map, spikes overlaid on the path, spatial autocorrelogram and 2D Fourier spectrogram of a grid cell recorded on the first and second days ((A), top & bottom rows, respectively); corresponding cluster and spike waveforms shown in blue in (C) & (D)). (B) Similar plots for a simultaneously recorded neighbouring grid cell on the first and second days ((B) top & bottom rows respectively). Its cluster and spike waveforms shown in red, (C) & (D). The similarity of waveforms from one day to another of both of the cells and the similarity of firing pattern of the grid cell in (B) strongly suggest that the blue cluster in ((C), first day) and ((D) second day) correspond to the same cell. The third tetrode channel was lost on the second day of the recordings. (E) temporal autocorrelogram of the grid cell in (A) during the first trial, top, and the second trial, bottom.

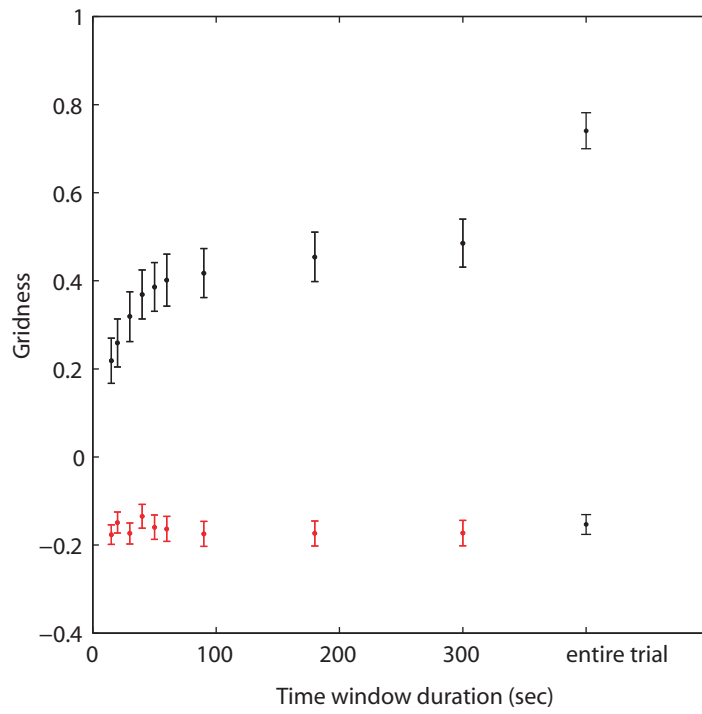


Fig. S13. The gridness of time windowed spatial autocorrelograms of grid cells (black) and other spatially periodic cells (red). The time windows used were: 15, 20, 30, 40, 50, 60, 90, 180, 300s. The minimum number of spikes per trial was 600. Notice that the grid scores of spatially periodic non-grid cells (red) do not increase with shorter time windows indicating that they are not temporally drifting grid patterns.

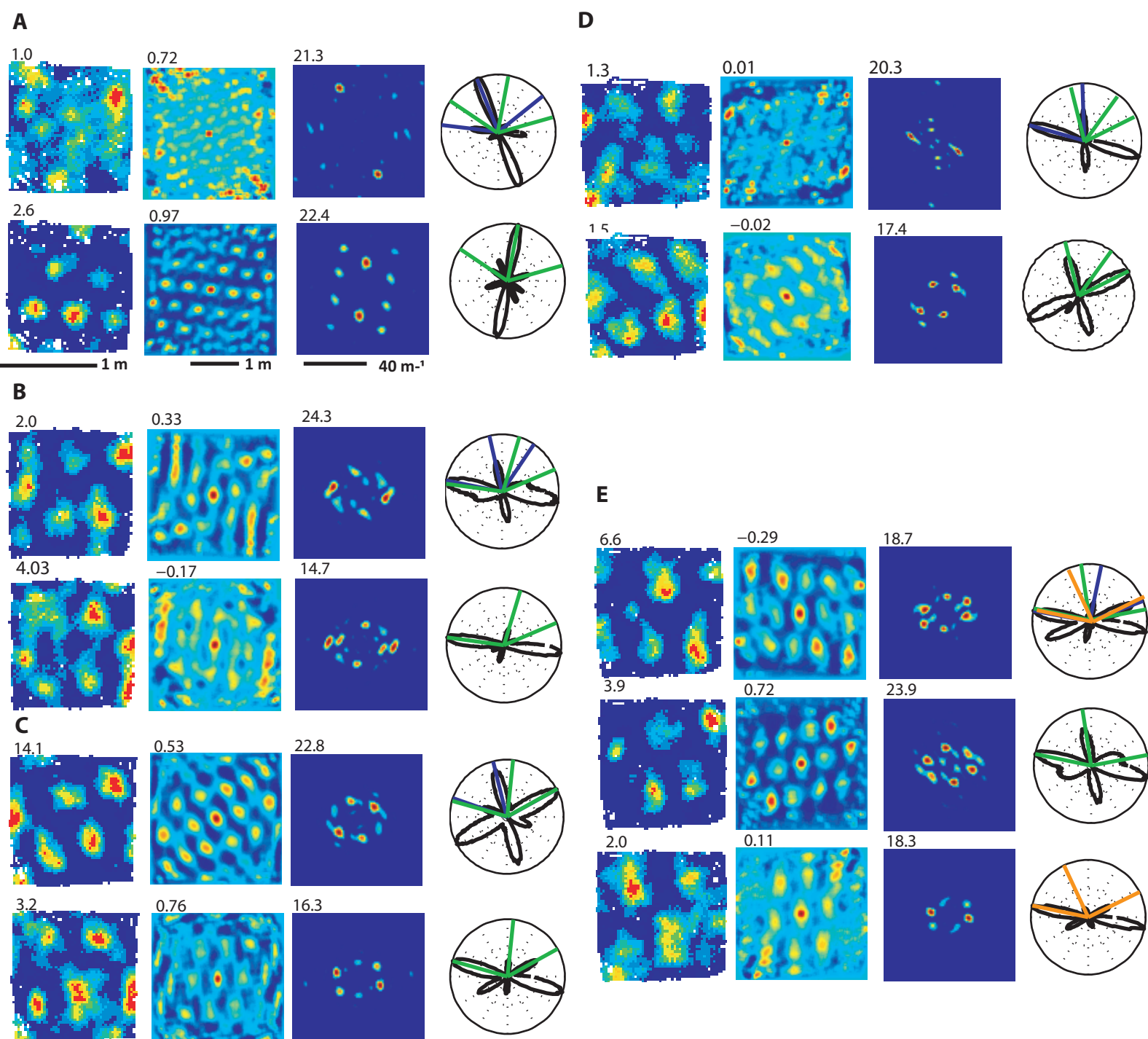


Fig. S14. Examples of simultaneously recorded cells which differ in the orientation of one or more Fourier components. A shows 2 grid cells with all components misaligned by 30°; B, a grid cell and an SPC with two of three components misaligned; C, 2 grid cells with 1 component misaligned; D, 2 SPCs with all components misaligned; E, one grid cell and 2 SPCs with two components misaligned.

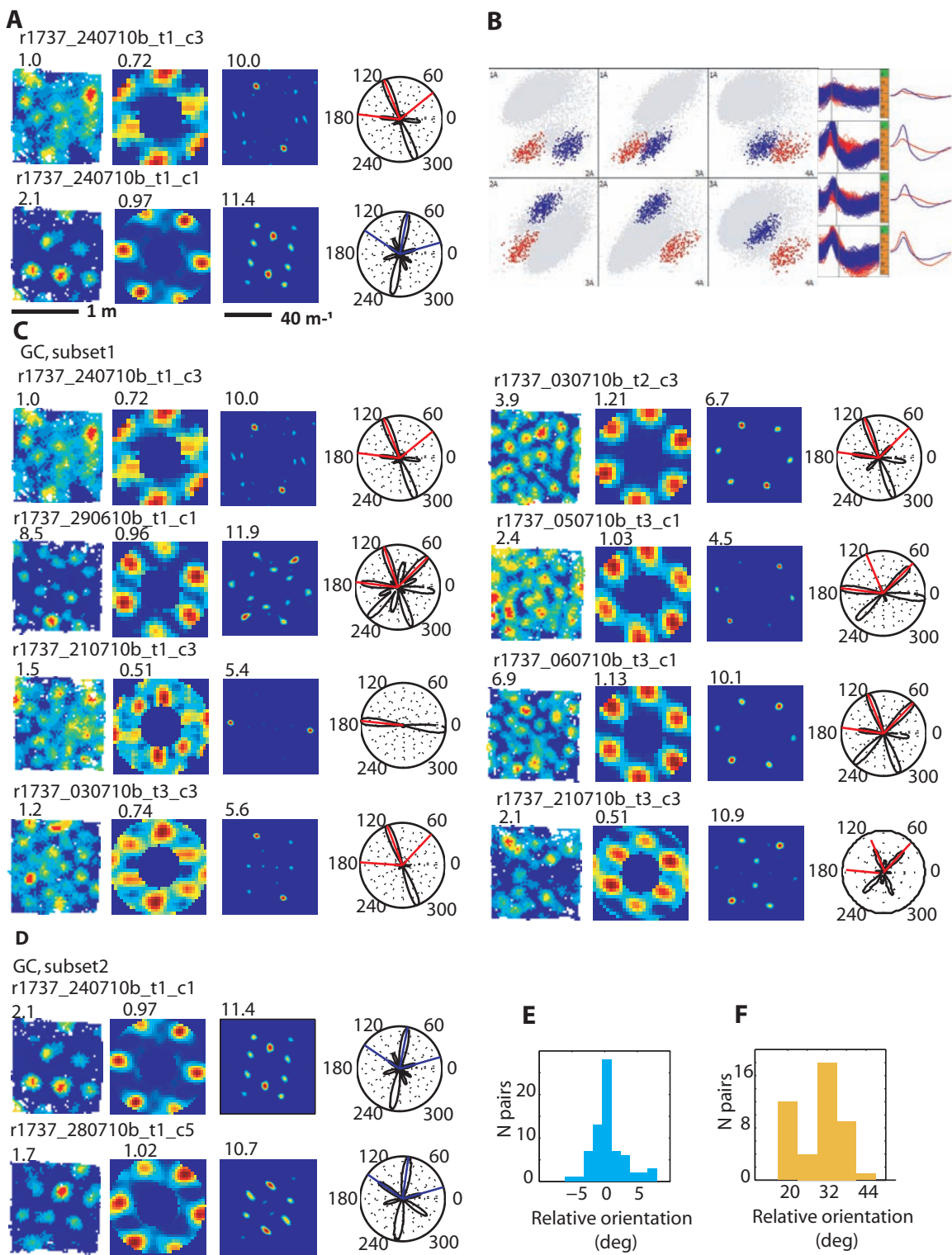


Fig. S15. Two distinct subsets of grid cells of different scale and orientation recorded from the same animal (r1737). (A) Two simultaneously recorded grid cells of different scale and orientation. (B) Clusters and waveforms of cells in a; cell1 in blue, cell3 in red. (C) All grid cells from subset1 (sharing scale and orientation with cell1); (D) all grid cells from subset2 (sharing scale and orientation with cell2). (E) Difference in orientation of the same component for cells within each subset. The mean difference equal to 0.74° ($t_{69}=-0.04^\circ$; $P=0.97$). (F) Difference in orientation between corresponding components between subsets. The mean difference is equal to 30.6° ($t_{43}=-0.01^\circ$; $P=0.99$).

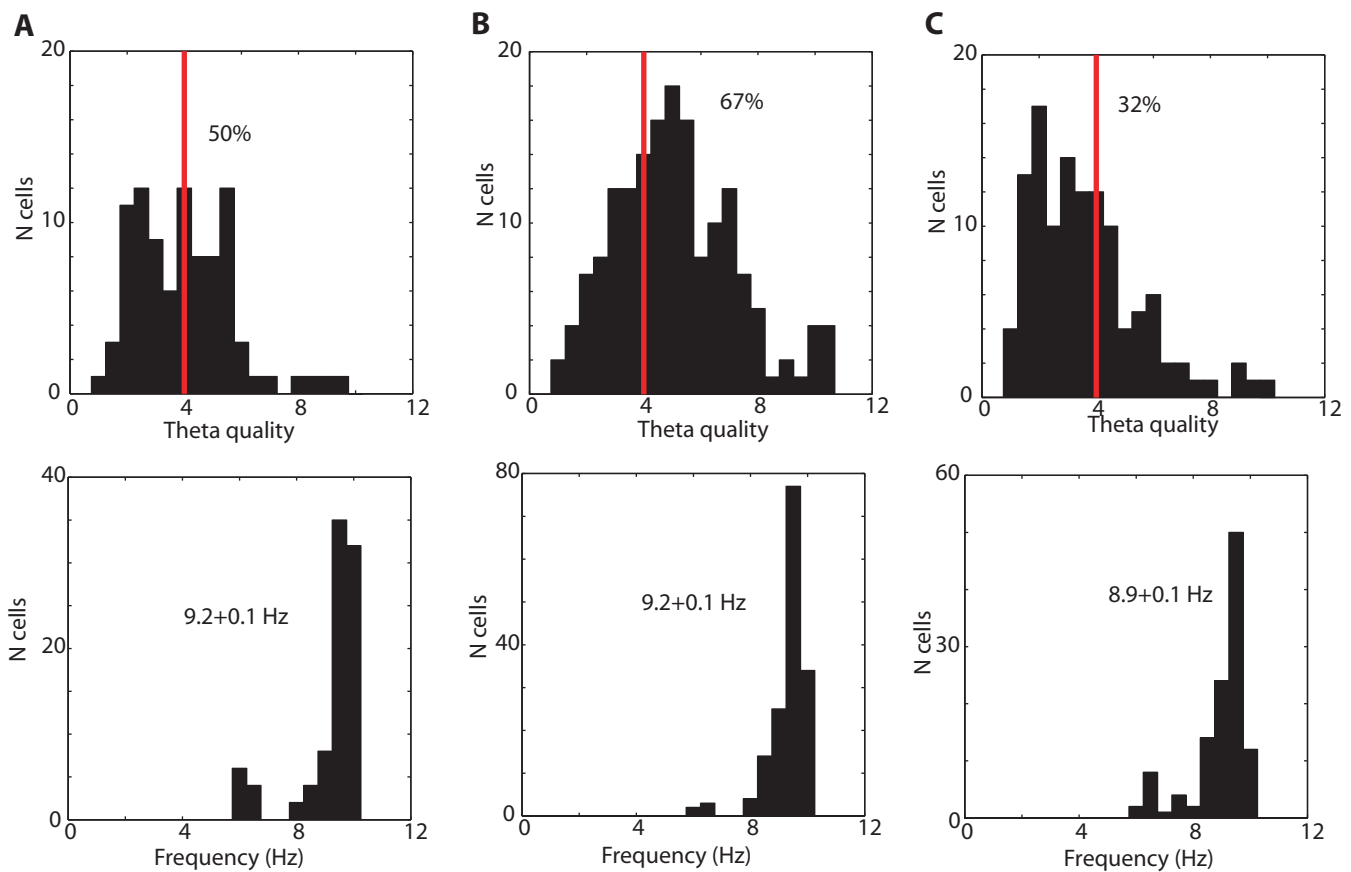


Fig. S16. Theta modulation of the firing of spatially periodic cells (SPCs) and non-SPCs. Cells were defined as theta modulated, if their θ score exceeded 4 (shown in red). (A) 50% of grid cells were theta modulated with mean frequency 9.2 ± 0.1 Hz (bottom). (B) 67% of non-grid cell SPCs were theta modulated with mean frequency 9.2 ± 0.1 Hz. (C) 32% of non-SPCs were theta modulated with mean frequency 8.9 ± 0.1 Hz (bottom).